THE RADIATION BALANCE OF THE EARTH FROM A SATELLITE

By

FREDERICK BISHOP HOUSE

NASW-65

A thesis submitted in partial fulfillment of the

requirements for the degree of

DOCTOR OF PHILOSOPHY

(Meteorology)

at the

UNIVERSITY OF WISCONSIN

1965

(1)

RQT-36066

ABSTRACT

The measurement of albedo and long-wave radiation by the black omni-directional sensor on TIROS IV satellite is used to study the radiation balance of the earth. The method used to obtain these results using only a single sensor system is developed. The principal results of this study are:

1. Accurate measurements of the solar and terrestrial radiation streams using a single sensing system are possible, providing the satellite orbit has a precessional period relatively long compared with the movement of weather systems.

2. Previous estimates of the meridional distribution of long-wave radiation agree remarkably well with satellite measurements.

3. Earlier estimates of the planetary albedo are confirmed. However, the meridional distribution of measured albedo values shows lower values in tropical latitudes and higher values at middle and polar latitudes than are indicated by previous estimates.

4. Because of 3. above, satellite measurements of the net radiation distribution with latitude require a larger transport of heat from tropical latitudes than previously estimated.

5. Finally, because separate measurements of solar input to the earth and radiative loss to space were available, the

possibility of global radiative equilibrium for a fraction of an annual period is considered.

ACKNOWLEDGEMENTS

My sincere thanks and appreciation go to the excellent staff of the Meteorology Department at the University of Wisconsin for providing my graduate education, and in particular to Professor Verner E. Suomi whose inspiration, advice, and guidance made possible the research in this thesis.

My thanks also go to the members of my reading committee, Professor H. H. Lettau and Associate Professor L. H. Horn, for their patience, understanding, and helpful suggestions in the preparation of this manuscript. In addition, thanks go to the other members of my committee, Professor R. A. Bryson for his helpful critique of my thesis and to Professor T. E. Houck of the Astronomy Department.

Appreciation and thanks go to my fellow working associates Dr. Peter M. Kuhn, Assistant Professor Don Johnson, Dr. William Shen, Dr. Seppo Huovilla, Mrs. Barbara Sparkman, Mr. Tom Vonder Haar, Mr. Steve Cox, and Mr. Dave Kauffman, whose stimulating discussions and helpful advice aided my research.

I want to acknowledge the many hours of work by Professor R. J. Parent and his staff of the Department of Electrical Engineering at the University of Wisconsin who processed miles of magnetic tape to extract the satellite data for this study.

The effort of designing, building, testing, launching, and receiving data from a satellite vehicle involves the work of

many people of the National Aeronautics and Space Administration. To them I am indebted.

This research was supported by the Division of Aeronomy and Meteorology, NASA Goddard Space Flight Center under contract NASW-65.

TABLE OF CONTENTS

LIST OF TABLES

LIST OF FIGURES

LIST OF SYMBOLS

(Listed in order introduced)

Symbol	Meaning	First used in equation number
LWR	Long-wave Radiation	Text
SWR	Short-wave Radiation	Text
ly/min	Radiant flux density (cal cm^{-2} min^{-1})	Text
ITC	Intertropical Convergence Zone	Text
ster	Steradian	Text
(I)	Night Orbit Position	Text
(II)	Shadow Transition Orbit Position	Text
(III)	Day Orbit Position	Text
R_s	Direct SWR from the sun	2.11
R_r	Reflected SWR from the earth	2.11
R_l	LWR from the earth	2.11
β	Solid angle subtended by the top of the atmosphere from the satellite	2.11
π	Effective cross sectional solid angle of a sphere	2.11
α_s	Sensor absorptivity to SWR	2.11
α_l	Sensor absorptivity to LWR	2.11
ϵ_l	Sensor LWR emissivity	2.11
σ	Stefan-Boltzmann's Constant	2.11
T	Temperature of the sensor	2.11

Symbol	Meaning	First used in equation number
θ_m	Maximum view half-angle subtended by the top of the atmosphere at the satellite	2.11
h	Height of the satellite above the earth's surface	2.11
r	Radius of the top of the atmosphere	2.11
RN_t	Net radiation at the top of the atmosphere	2.12
$^*\phi$	Zenith angle of the sun's rays at the subsatellite point	2.12
$\cos\ ^*\phi$	Correction for Incident angle of the sun's rays to the area viewed by the satellite	2.12
$(_t)$	Orbit position at the shadow transition	2.13
dRN_t	Absolute error in net radiation measurements	2.21
dR_s	Absolute error in direct SWR measurements	2.22
dR_r	Absolute error in reflected SWR measurements	2.23
dR_l	Absolute error in LWR measurements	2.23
$R_{l_{(I)}}$	Nighttime LWR loss	2.42
$\bar{R}_{l_{(I)}}$	Mean nighttime LWR loss along a latitude	2.43
$\bar{A}$	Mean albedo of the earth-atmospheric system	2.44
$\bar{R}_{l_{(III)}}$	Mean daytime LWR loss along a latitude	2.44

Symbol	Meaning	First used in equation number
$\overline{RN}_t$	The net radiation for an average day along a latitude	2.47
$\overline{R}_s$	Mean solar energy incident on a horizontal surface at the top of the atmosphere	2.47
i	Summation index	2.52
n	Number of observations	2.52
C_m	Lumped mirror radiation constant	3.21
C_c	Lumped post conduction constant	3.21
C_t	Lumped thermal lag constant	3.21
T_m	Temperature of the mirror	3.21
$\overline{T}$	Mean sensor temperature between observations	3.22
$\overline{T}_m$	Mean mirror temperature between observations	3.22
$\epsilon_1(\overline{T})$	LWR emissivity as a function of sensor temperature	3.22
$\alpha_1(250^oK)$	Constant LWR absorptivity at 250^oK	3.22
m	Number of latitude zones	4.311
PT_i	Planetary heat transport across the i^{th} zone	4.311
A_z	Area of the i^{th} zone	4.311
$\emptyset$	Zenith angle of the sun at a point on the earth	Appendix
k	Number of solid angle cones defined by β	Appendix

I. INTRODUCTION

Incoming and outgoing radiation fluxes at the outer fringes of the atmosphere are the means of energy exchange between the sun, the planet earth and space. The planet earth receives short-wave radiation, SWR, from the sun, principally in the wavelength region 0.2μ to 3.5μ . A portion of the solar irradiance is reflected back to space, and the rest is absorbed by the earth-atmospheric system. The earth loses energy to space by thermal emittance of long-wave radiation, LWR, at wavelengths greater than 4.0μ . This energy exchange with space is the radiation balance or net radiation at the top of the atmosphere. Now, we can obtain global net radiation measurements from satellites.

Before using satellite observations in a study of the earth's radiation balance, we must establish confidence in the measurements. In laboratory experiments, for example, calibration of instruments is possible before and after observations, to check for instrumental changes with time. For satellite instruments, direct calibration after launch is not possible. In-flight calibration in space is desirable to determine any instrumental changes.

The research in this thesis demonstrates the potential space calibration of satellite instruments using a single,

spherical radiometer. It is shown that accurate observations of net radiation are possible from one sensor and that the solar and terrestrial radiation streams can be separated individually into meridional averages of albedo and long-wave radiation. One advantage of a single sensor system is its accuracy, because relative errors in one sensing system will ordinarily be much smaller than absolute errors in two systems. Furthermore, it is shown that the sensor can be space calibrated.

With satellite observations we can study the meridional distribution of net radiation which is the driving force behind the general circulation. Net radiation, positive at low latitudes and negative at high latitudes, is an essential feature in the atmosphere's thermodynamic engine. The magnitude of the north-south gradient of the net radiation defines the meridional transport of heat which the general circulation must deliver. We are in a new position to compare observed results with values previously calculated.

This thesis is divided into three parts: 1) The scheme and potential accuracy of measurements by a one sensor system are discussed. 2) The design of the specific sensors used on TIROS IV, the method used to calculate net radiation using only its black sensor, and the accuracy of the measurements are treated. 3) Section IV contains a summary of TIROS IV measurements, and Section V contains a discussion of the conclusions.

II. THE NET RADIATION OF THE EARTH FROM A SATELLITE

A satellite vehicle provides us with an observational platform outside the earth's atmosphere that can operate for extended periods of time[1]. Observations of the radiative exchange at the top of the atmosphere are possible for all areas of the earth. Measurements, however, are not synoptic as are ordinary weather observations.

The so called top of the atmosphere is a spherical surface, arbitrarily chosen at a height of 30 km above the earth's surface. It is defined by the radius, r , in Figure 2. Less than one per cent of the atmosphere remains between this level and space; therefore, satellite measurements, normalized to this level, are representative of the radiation transfer between the planet earth and space.

There is a strong local time variation of net radiation at any point on the earth. The net radiation is defined as the difference between the absorbed and the emitted radiant flux densities. The absorbed SWR is dependent on the cosine of the zenith angle of the sun's rays at any point, whereas the outgoing LWR is relatively constant during both the day and night. In general we can expect positive values of net radiation during the day and negative values during the night.

---

[1] For example, Stroud and Nordberg (1956), Widger (1957), Godson (1958), Suomi (1958), and Wexler (1960).

The problem of earth sampling from a satellite is to describe the daily value of net radiation from observations obtained during satellite passage. The local time of satellite passage over a given latitude depends on the orbit position with respect to the sun as shown in Figure 4. Any satellite orbit, inclined to the earth's equator, precesses with time (a true polar orbit is an exception). Therefore, the local time of net radiation measurements along a latitude will change with sun-orbit position. We make use of this property in the discussion of Section 2.3 to obtain the daily total net radiation along a latitude.

2.1 Measurement of Solar and Terrestrial Radiation Using a Single Spherical Sensor

Suppose an isolated sphere is in an orbit around the earth. Figure 1 shows three positions in the sphere's orbit that have different sources of incident radiation. These orbit positions are hereinafter denoted (I), (II), and (III).

(I) one source - only LWR from the earth (in the earth's shadow).

(II) two sources - LWR and direct SWR near the shadow transition.

(III) three sources - LWR, direct SWR and reflected SWR from the earth.

Let assume further that this spherical sensor has zero heat capacity, and that its spectral absorptivity to SWR and to LWR is uniform. The balance of energy gains and lossed by the sensor is

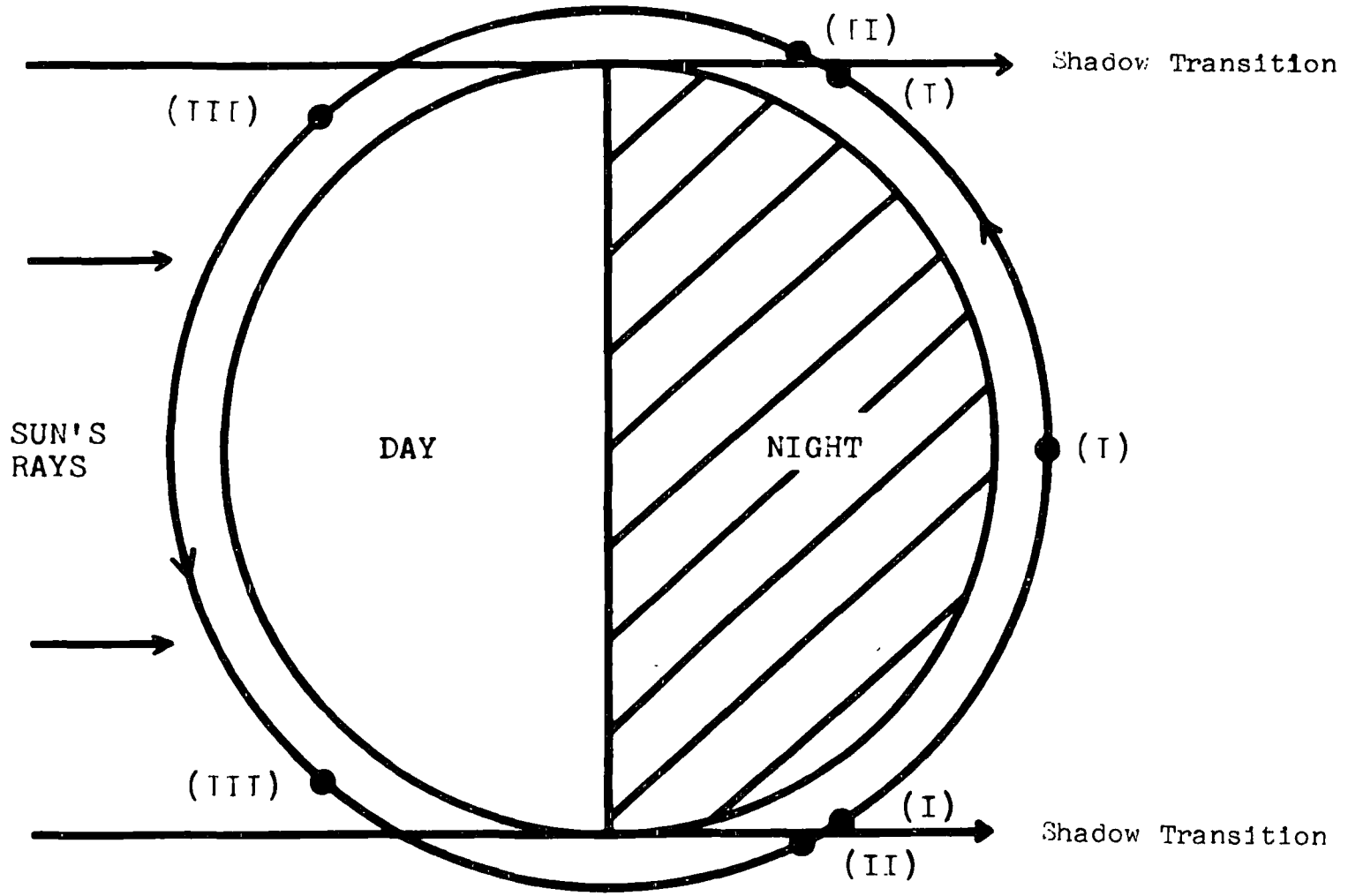

Figure 1

Cross Sectional View of a Satellite Orbiting the Earth.

$$\alpha_s \pi R_s + \alpha_s \beta R_r + \alpha_l \beta R_l = 4 \pi \varepsilon_l \sigma T^4 , \qquad (2.11)$$

where R_s = direct SWR from the sun,

R_r = reflected SWR from the earth,

R_l = LWR from the earth,

α_s = the absorptivity to SWR (0.2 to 3.5μ),

α_l = the absorptivity to LWR ($>4.0\mu$),

ε_l = the LWR emissivity ($>4.0\mu$),

β = $2\pi(1-\cos\theta_m)$ as explained in Figure 2 is the solid angle subtended by the top of the atmosphere at the satellite.

σ = Stefan-Boltzmann's constant,

T = the sensor's temperature in ^{o}K , and

r = 6405 km.

It is possible to simplify (2.11) further since $\alpha_s = \alpha_l = \varepsilon_l$ using Kirchoff's Law. Equation (2.11) relates the sensor's temperature to the magnitude of the incident radiation streams. The solid angle β depends on satellite height and geometrically normalizes measurements from an elliptical orbit at the satellite to the 30 km top of the atmosphere.

Figure 3 shows typical values of the ideal sensor's temperature as it orbits the earth, where R_s = 2.00 ly/min, R_l = 0.33 ly/min (isotropic radiation field), and the albedo is uniformly 35 per cent. The orbit positions in Figure 3 correspond to those in Figure 1.

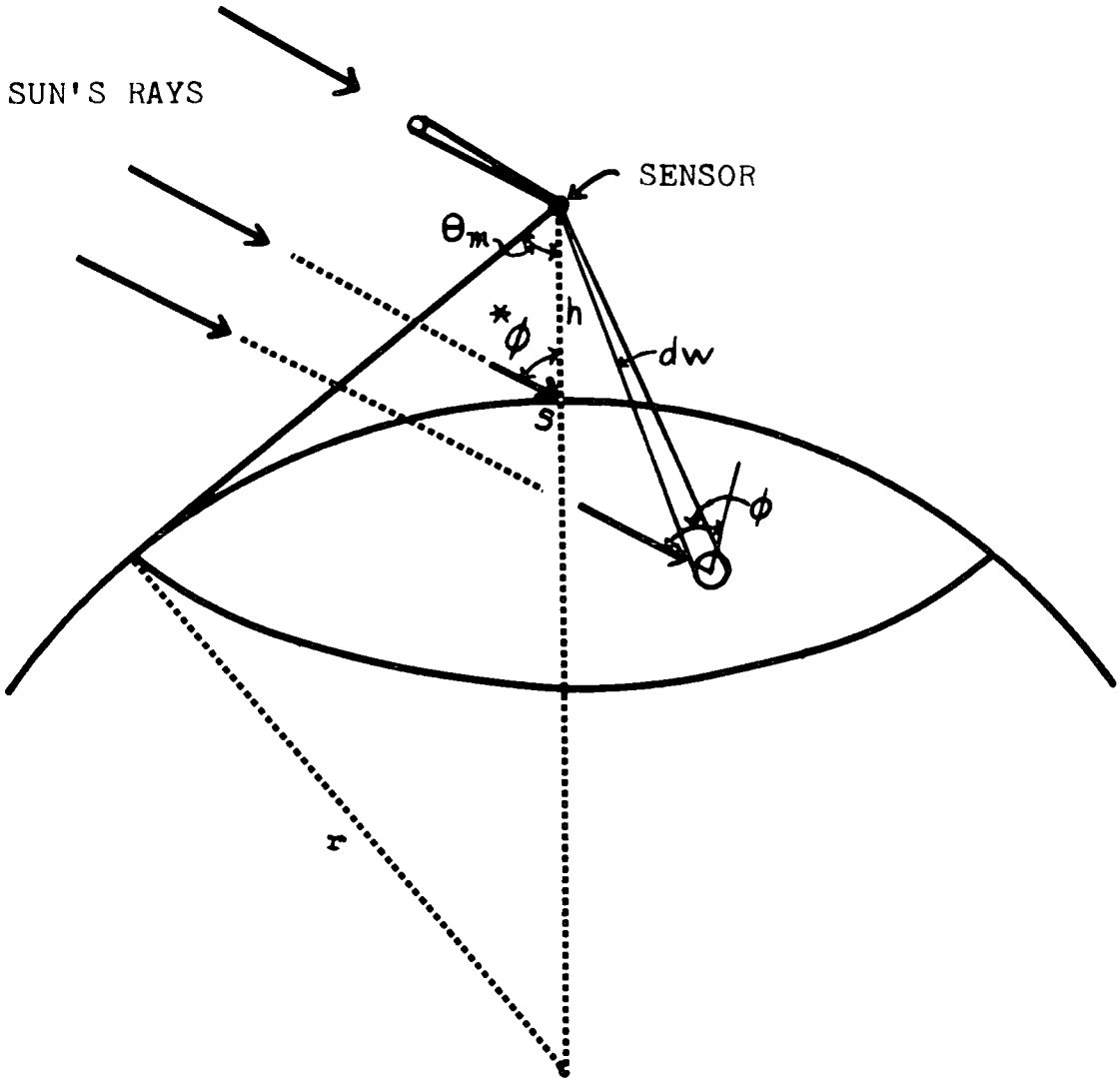

Satellite Geometry.

Figure 2

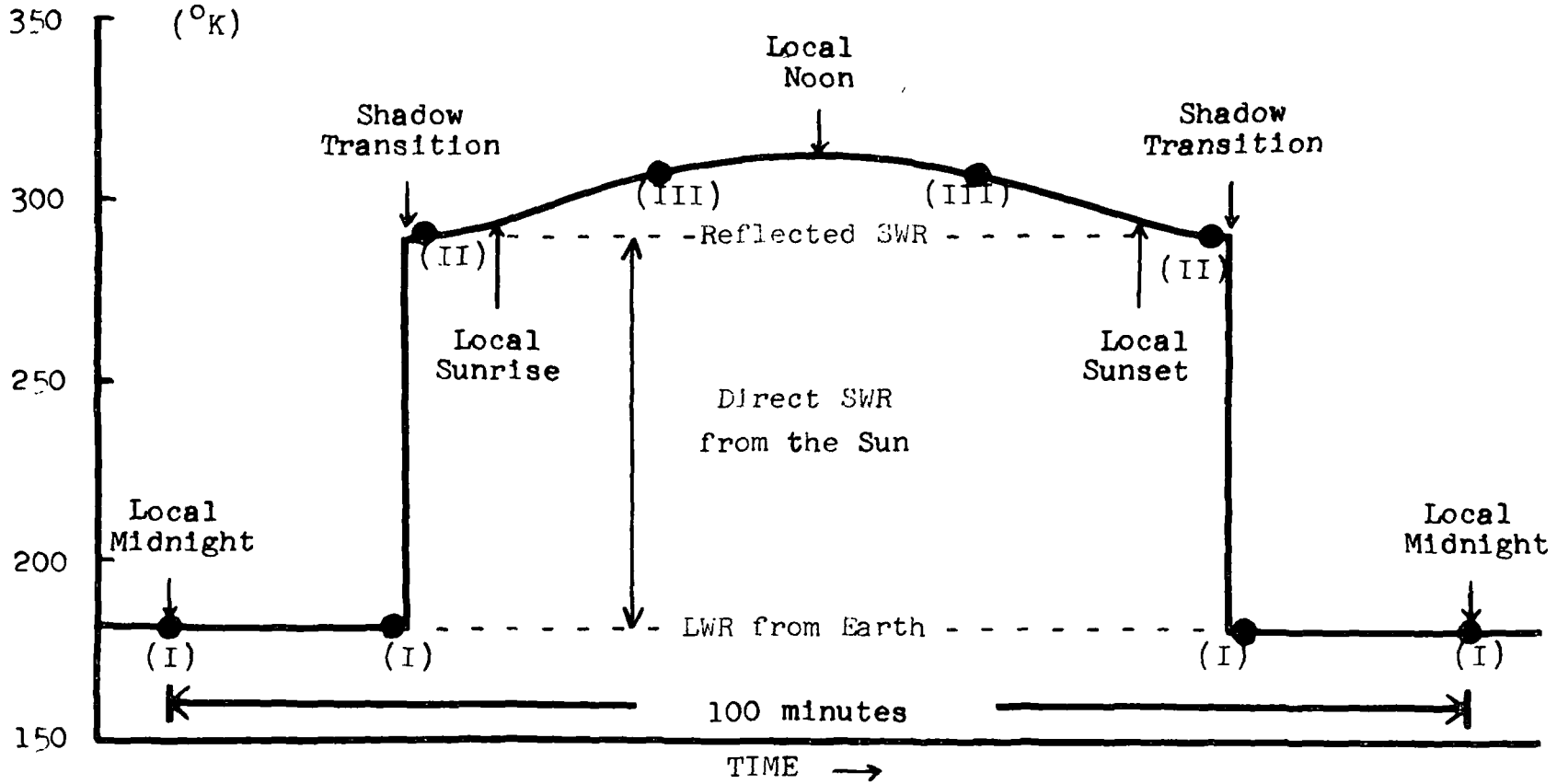

Figure 3

Temperature Variation of an Ideal Satellite Orbiting the Earth.

Orbit Specifications: Satellite Height = 800 km. Orbit Inclination = 48 deg. Date is March 21. Local Noon is at the Vernal Equinox.

The three sources of radiation incident on the sensor are quite evident from the temperature variation. They are the LWR from the earth (I), the direct solar radiation observed at the shadow transition (II), and the additional reflected SWR from the earth during (III).

The net radiation at the top of the atmosphere, RN_t, for the area viewed by the satellite is

$$RN_t = \cos {}^{*}\phi \, R_s - (R_r + R_l). \qquad (2.12)$$

The function $\cos {}^{*}\phi$ geometrically weights the direct SWR, R_s, which is incident to the area viewed by the satellite. The mathematical interpretation of this function is discussed in the Appendix. The direct solar irradiance, R_s, is

$$R_s = 4 \, (\sigma T_{(II)}^{4} - \sigma T_{(I)}^{4})_t \quad , \qquad (2.13)$$

where the temperature subscripts $_{(II)}$ and $_{(I)}$ define the orbit positions at the shadow transition subscript $_t$. Since R_s is measured, the solution for the reflected and emitted irradiances from the earth during the sunlit half of the orbit, (III), is

$$(R_r + R_l) = \frac{\pi (4 \sigma T^4 - R_s)}{\beta} \qquad (2.14)$$

Substituting (2.13) and (2.14) into (2.12) yields the net radiation for the area viewed by the satellite at any time.

$$RN_t = \frac{4\ (\beta\ \text{Cos}\ {}^{*}\emptyset + \pi)\ (\sigma T_{(II)}{}^{4} - \sigma T_{(I)}{}^{4})_t}{\beta} - \frac{4\ \pi\ \sigma T^4}{\beta} \qquad (2.15)$$

2.2 Error Analysis of Net Radiation Measurements

Because values of net radiation may be both positive and negative, the discussion of errors below treats only the absolute error of the measurements. To assess the errors, we differentiate (2.12) obtaining

$$dRN_t = \text{Cos}\ {}^{*}\emptyset\ dR_s - d\ (R_r + R_l)\ , \qquad (2.21)$$

where the differentials represent the absolute errors for individual terms of (2.12). From (2.13), dR_s in (2.21) is

$$dR_s = 4\ (d\ \sigma\ T_{(II)}{}^{4} - d\ \sigma T_{(I)}{}^{4})\ , \qquad (2.22)$$

and from (2.14), $d\ (R_r + R_l)$ is

$$d\ (R_r + R_l) = \frac{4\ \pi\ d\ \sigma T^4 - \pi\ dR_s}{\beta}\ , \qquad (2.23)$$

where from Kirchoff's Law the absorptivities are equal to the emissivity. From (2.22) and (2.23) it is evident that the accuracy of the measurement depends only on the sensor's temperature and is independent of the absorptivities or emissivity.

Let us assume a reasonable uncertainty of $\pm 0.2^{\circ}C$ in the measurement of the sensor's temperature. Since this error is systematic, it will be either positive or negative for all temperatures of the sensor. Using a solid angle of 3.4 steradians for β and typical temperatures in Figure 3, from (2.22) the absolute error for direct SWR is

$$|d\ R_s| = 4(.0016 - .0004) = .0048 \text{ ly/min},$$

and from (2.23), using $T = 305^{\circ}K$, the absolute error of reflected and emitted irradiances is

$$|d\ (\ R_r + R_l\ )| = \frac{12.57 \times .0019 - 3.4 \times .0048}{3.4}$$

$$= .0026 \text{ ly/min.}$$

The absolute error in the net radiation measurement is

$$|dRN_t| = \text{Cos}\ ^{*}\emptyset \times .0048 - .0026 \text{ ly/min.}$$

The function $\text{Cos}\ ^{*}\emptyset$ can vary from 0.986 when the satellite is at local noon to 0.0 at the shadow transition; therefore, the error in single values of RN_t is .0021 to -.0026 ly/min. Because the error is both positive and negative for different values of $\text{Cos}\ ^{*}\emptyset$, the error in mean values of $\overline{RN}_t$ is negligible.

Measurements using a one sensor system possess a high degree of accuracy since errors are relative and tend to cancel.

2.3 Local Time Sampling of Net Radiation

The orbit of a typical meteorological satellite like TIROS IV precesses westward with respect to the sun as shown in Figure 4 (NASA Staff Members, 1963). For example, in Figure 4 (b) satellite local noon is near the equator on Feb. 23. Sixteen days later 4 (c) local noon is in the southern hemisphere, seventeen days later 4 (d) it is close to the equator again, etc. The period for one precessional cycle of TIROS IV satellite is about 66 days.

As mentioned perviously, the net radiation varies with local time as shown in Figure 5. The problem is to describe the daily value of net radiation along a latitude from a sample of observations obtained during different time passages of the satellite. To fulfill the 24 hour local time sampling requirement of a representative net radiation sample, we must extend the averaging period of observations to one precessional cycle. Therefore, the measurement of net radiation from our ideal satellite represents an average day during the precessional cycle.

Clearly at any one location the weather may be vastly different for those days early in the cycle when the morning local

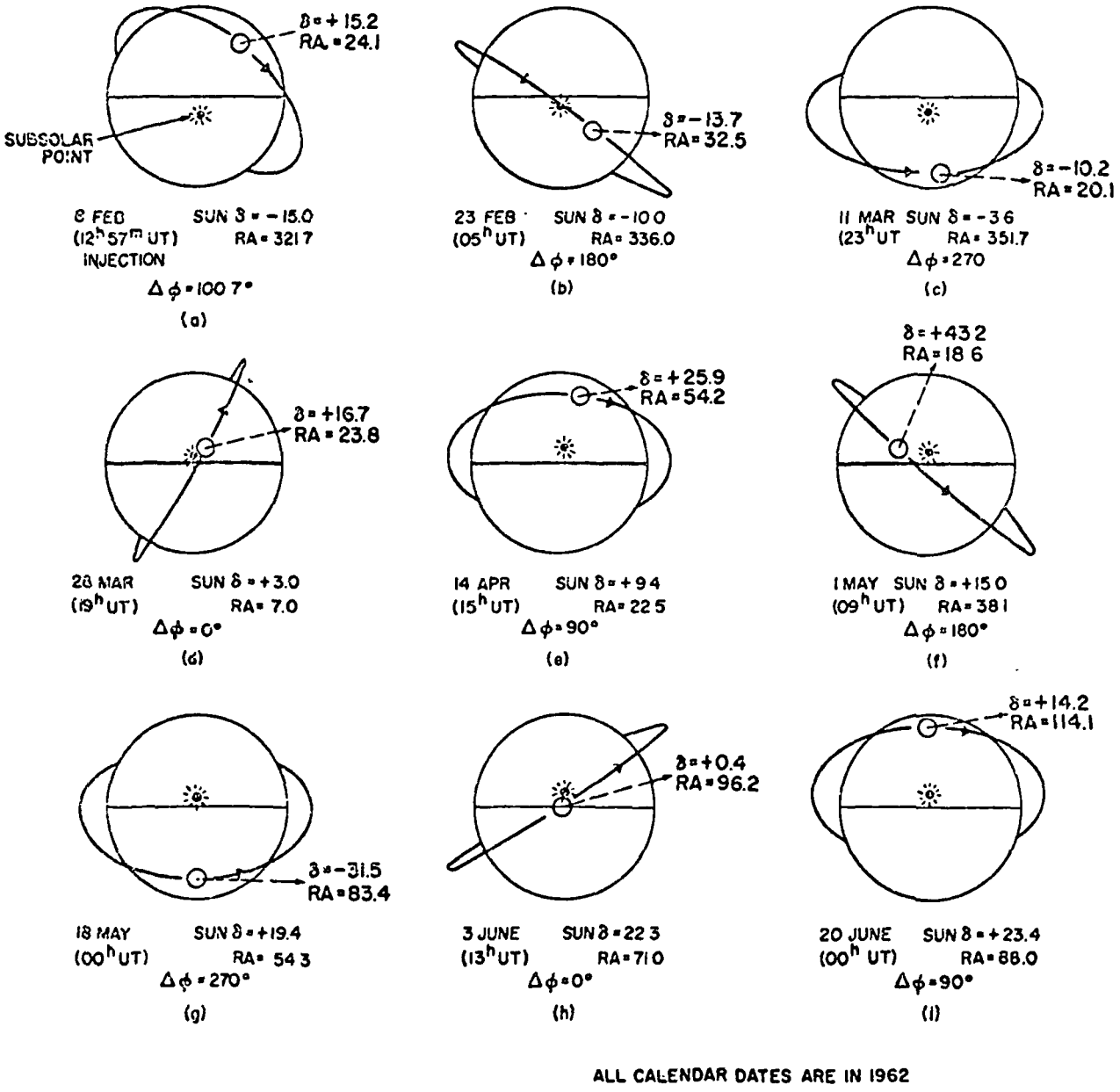

Figure 4 (*a*, *b*, *c*, *d*, *e*, *f*, *g*, *h* and *i*)—Cosmic view of the earth and the precessing TIROS IV orbital plane. The celestial coordinates of the sun and the satellite spin vector are shown for each selected day. The time is given to the nearest hour GMT and corresponds to the given value of $\Delta\phi$.

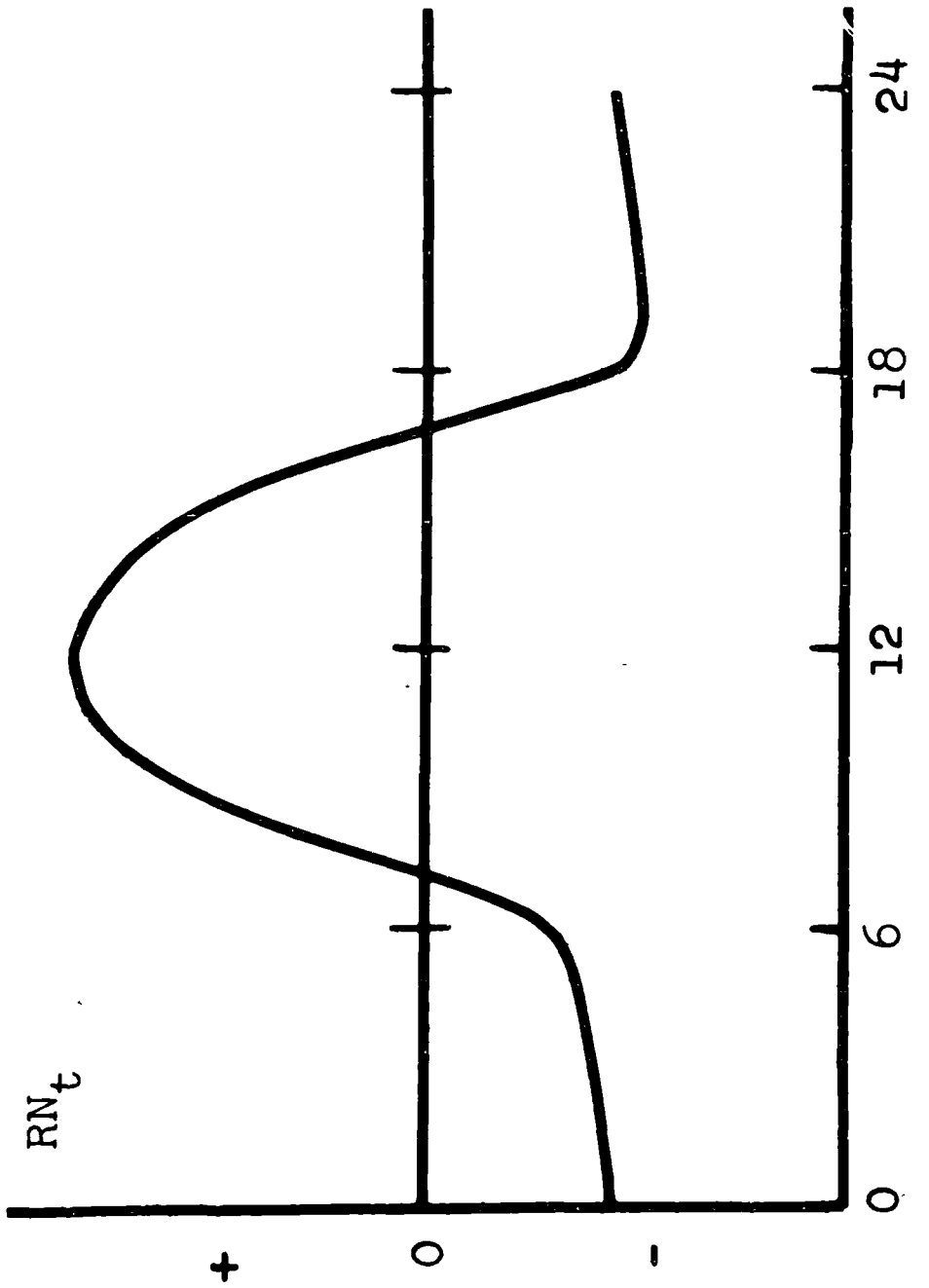

Figure 5

Qualitative Nature of the Diurnal Variation of Net Radiation.

times are being sampled, as compared to those days late in the precessional cycle when the afternoon hours are being sampled. Thus the net radiation measurements for any one station are highly unrepresentative. However, since a large part of the atmospheric motion is zonal and we are taking averages around a latitude circle, we would expect to sample clear, cloudy and intermediate weather situations around the latitude with equal frequency for each value of local time. The positions of the storm systems and the position of the subsatellite point are independent, thus no artificial weighting of particular storm systems is likely to occur.

2.4 Separation of the Solar and Terrestrial Radiation Components

The scheme to measure net radiation in Section 2.1 using a single spherical sensor requires that the absorptivities of the sensor's surface to SWR and to LWR are the same. This requirement is necessary because the reflected and emitted irradiances from the earth, $(\alpha_s \beta R_r + \alpha_l \beta R_l)$ in (2.11), must be given equal weighting, otherwise a bias is introduced into the measurements. The black paint on the TIROS IV sensor is not gray as in the ideal sphere, i.e. α_s is not equal to α_l, therefore, the theory developed below includes variable absorptivities.

In this section we show that it is advantageous to separate the solar and terrestrial radiation streams, using only one sensor, into the latitudinal averages of albedo and LWR so that the average net radiation along a latitude can be calculated. However, in order to calculate the net radiation using albedo and LWR values, we must assume a value for the solar constant. Essentially we are trading off the assumed solar constant in the calculations to meet the requirement for a variable absorptivity. On the other hand, our averages along a latitude are no longer restricted to a period of one precessional cycle. As will be shown later, accurate measurements of LWR, albedo, and net radiation are still possible using a single sensor.

Let us consider the more general form of the energy balance equation (2.11) where the absorptivities are variable. Dividing (2.11) by α_1, we have

$$\frac{\alpha_s}{\alpha_1} \pi R_s + \frac{\alpha_s}{\alpha_1} \beta R_r + \beta R_l = 4\pi \frac{\varepsilon_1}{\alpha_1} \sigma T^4. \qquad (2.41)$$

The calculation for LWR at night is

$$R_{l(I)} = \frac{4\pi \varepsilon_1 \sigma T^4}{\alpha_1 \beta} . \qquad (2.42)$$

The mean LWR loss along a latitude during an averaging period, $\bar{R}_{1(I)}$, is

$$\bar{R}_{1(I)} = \frac{\sum_{i=1}^{n} (R_{1(I)})_i}{n} , \qquad (2.43)$$

where n is the number of observations during the period.

The solar irradiance term, $\frac{\alpha_s}{\alpha_1} R_s$, calculated as in (2.13), is known each time at the shadow transition. The incident solar radiation illuminating the earth at any given time is $2 (1 - \cos \theta_m) \cos^{*}\phi \frac{\alpha_s}{\alpha_1} \pi R_s$. The term for direct solar irradiance can be subtracted from every daytime observation in (2.41) leaving the reflected and emitted irradiances from the earth $\beta (\frac{\alpha_s}{\alpha_1} R_r + R_{1(III)})$. We must still separate $R_{1(III)}$ from $\frac{\alpha_s}{\alpha_1} R_r$. If we assume that day and night LWR averages are equal, i.e. $R_{1(III)}$ is equal to $R_{1(I)}$, the summed component of $\frac{\alpha_s}{\alpha_1} R_r$ can be isolated by a simple subtraction of averages. This assumption is discussed later in Section 3.4. On this basis, the mean albedo $\bar{A}$, which is an average around the earth, along a latitude circle and during an averaging period, is

$$\bar{A} = 100 \frac{\sum_{i=1}^{n} (\beta \frac{\alpha_s}{\alpha_1} R_r + R_{1(III)})_i - \bar{R}_{1(I)} \sum_{i=1}^{n} \beta_i}{\sum_{i=1}^{n} \left[(1 - \cos \theta_m) \cos^{*}\phi \frac{\alpha_s}{\alpha_1} \pi R_s \right]_i} . \qquad (2.44)$$

It is easier to understand (2.44) if further simplifications are made. Carrying out the subtraction in the numerator and dividing by the summation of β_i, we have

$$\overline{A} = 100 \; \frac{\sum_{i=1}^{n} \left(\frac{\alpha_s}{\alpha_1} R_r \right)_i}{\sum_{i=1}^{n} \left(\cos^{*}\phi \, \frac{\alpha_s}{\alpha_1} R_s \right)_i} \; . \qquad (2.45)$$

The absorptivity ratio, $\frac{\alpha_s}{\alpha_1}$, cancels in (2.45) since the same sensor measures both the direct and reflected SWR irradiances. Consequently the albedo calculation is independent of absorptivity values, even for a surface whose spectral absorptivity varies with wavelength. Equation (2.45) reduces in final form to

$$\overline{A} = 100 \; \frac{\sum_{i=1}^{n} \left(R_r \right)_i}{\sum_{i=1}^{n} \left(\cos^{*}\phi \, R_s \right)_i} \; . \qquad (2.46)$$

Equation (2.46) states that the mean albedo along a latitude circle is the sum of the reflected irradiances divided by the sum of the solar inputs and shows that the calculation is independent of the absorptivity ratio $\frac{\alpha_s}{\alpha_1}$.

The net radiation for an average day along a latitude circle, $\overline{RN}_t$, is

$$\overline{RN}_t = \frac{100 - \bar{A}}{100} \bar{R}_s - \bar{R}_{1(I)} \qquad (2.47)$$

$\bar{R}_s$ is the average solar input of energy incident on a horizontal surface at the top of the atmosphere, based on a solar constant of 2.00 ly/min (Johnson, 1954).

2.5 Error Analysis of LWR and Albedo Measurements

The accuracy of the albedo and LWR averages is determined entirely by the accuracy of the sensor temperature measurement. A typical temperature uncertainty of $\pm$ 0.2 ^{o}K yields an absolute error in nighttime LWR averages of

$$\left| d\, R_{1(I)} \right| = \frac{4\pi\, d\, \sigma\, T^4}{\beta} = \frac{12.57 \times .0004}{3.4} = .0015 \text{ ly/min.} \qquad (2.51)$$

For typical values of LWR this uncertainty is only $\pm$ 0.5 %.

When assessing the error in albedo averages, it is convenient to consider (2.44) in symbolic notation, where

$$X = \sum_{i=1}^{n} \frac{\beta \left(\frac{\alpha_s}{\alpha_1} R_r + R_{1(III)} \right)_i}{n}, \quad Y = \frac{\bar{R}_{1(I)} \sum_{i=1}^{n} \beta_i}{n}, \text{ and}$$

$$Z = \sum_{i=1}^{n} \frac{\left((1 - \cos \phi_m) \cos^{*} \phi \frac{\alpha_s}{\alpha_1} \pi R_s \right)_i}{n} .$$

$$\bar{A} = 100 \frac{X - Y}{Z} . \qquad (2.52)$$

Differentiating (2.52), we have

$$d\bar{A} = 100 \frac{(ZdX - XdZ - ZdY + YdZ)}{Z^2} . \qquad (2.53)$$

Typical average values for (2.44) are X = 2.80, Y = 1.20, and Z = 4.70 (ster-ly/min). The differentials are the errors for day calculatlons, dX and dZ, for night calculat ons, dY and for the absolute error in the albedo, $d\bar{A}$. Since dX = dZ, (2.53) reduces to

$$d\bar{A} = 100 \left(\frac{dX (Z - X + Y) - ZdY}{Z^2} \right) . \qquad (2.54)$$

Assuming the worst case where dX and dY are opposite in sign, .0200 and -.0045 ly/min respectively, the computed error would be

$$d\bar{A} = 100 \frac{.020 (4.70 - 2.80 + 1.20) + 4.70 \times .0045}{22.1} = 0.8\%.$$

The albedo error will vary with latitude of observation since Y in (2.52), the LWR term, is a function of latitude. A reasonable estimate of the albedo error for all latitudes is one per cent (an absolute error in albedo per cent).

Thus an isolated sphere orbiting the earth is capable of yielding highly accurate measurements of the average albedo and LWR of the earth, assuming that the temperature measurement is accurate to $\pm$ 0.2 ^{o}K. One might consider a similar configuration for future satellites.

An error analysis of average net radiation measurements along a latitude is discussed in Section 3.4, after a discussion of the actual measurements made by the black omni-directional sensor on TIROS IV satellite.

III. MEASUREMENTS FROM TIROS IV SATELLITE

The University of Wisconsin heat balance experiment on TIROS IV satellite consists of two sensors with different absorbing surfaces; one sensor has a black surface and the other sensor has an anodized aluminum or "white" surface. Suomi (1958, 1961), Bignell, (1961), and Malkevich, et. al. (1962) have discussed the two sensor experiment in detail. With this dual sensing system individual measurements of albedo and LWR are obtained throughout the orbit. Here we treat only one sensor, the black hemisphere, on TIROS IV in a manner similar to the ideal spherical sensor discussed in the previous section.

3.1 Sensor Construction and Design

The TIROS IV sensor shown in Figure 6 consists of a hemisphere and mirror instead of a sphere. The mirror prevents the hemisphere from "seeing" the carrying space craft. The sensor is constructed from thin aluminum sheeting formed into a hemispheric shell. A thermistor is used to measure its temperature. A perforated titanium post using a balsa wood insert of low thermal conductivity supports the shell above a four-inch diameter aluminized mirror.

Two sensor-mirror systems, each containing a black and an anodized sensor, are mounted opposite each other on extended

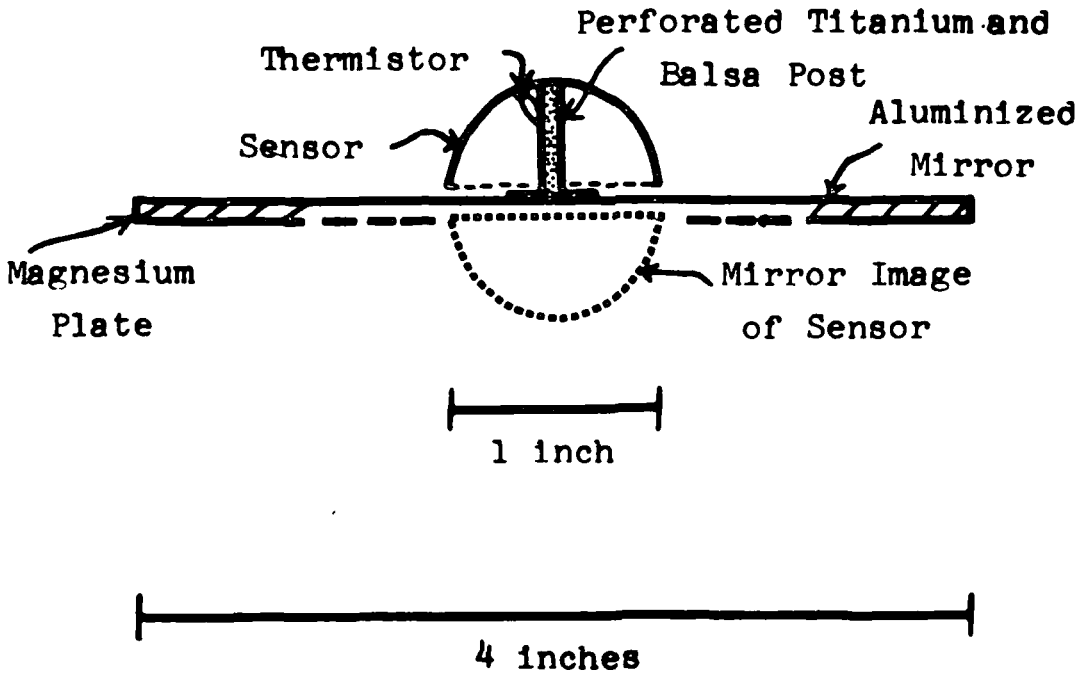

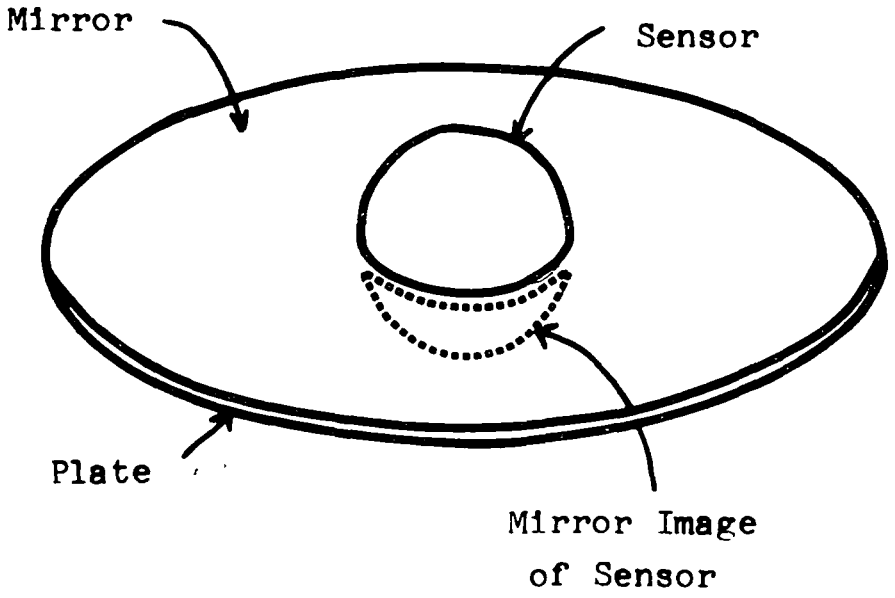

Sketch of the TIROS IV Sensor-Mirror System.

Figure 6

booms from the lower part of the satellite's body. The planes of the mirrors are positioned at a fixed angle to a line which is normal to the spin axis of the satellite.

The mirrors shield each sensor from direct radiation emitted by the other sensors and from radiation emitted by the satellite's body. As the satellite rotates on its axis, a portion or all of one sensor may be eclipsed from direct view with the earth. However, the matched sensor on the opposite side of the satellite starts viewing the earth in the same manner as the first sensor when it is eclipsed. Therefore, the sensors on TIROS IV are two hemispheres (essentially a severed sphere) which are positioned on opposite sides of the satellite vehicle and are protected from unwanted satellite radiation by the mirrors.

The sensor temperatures are measured by thermistors, fastened with epoxy cement to the inside of the hemispheric shells. Ideally, the temperature of each sensor should be monitored continuously. However, telemetry requirements limited the number of possible observations, and to reduce the total number of measurements, matched pairs of thermistors are connected in series for similar sensors on opposite sides of the spacecraft. Therefore, the measured sensor temperature received from the satellite is an average of two temperatures from matched thermistors. When the satellite spin period is short compared to the sensor's time

constant, the measured average temperature can be taken to represent the temperature of a single hemisphere.

The information telemetered to earth includes information on the temperatures of the mirrors and sensors and on a fixed resistance value which allows one to compensate for drift of the electronics in the satellite.

3.2 Energy Balance Equation for the TIROS Sensor

With an energy balance equation we relate the sensor's temperature to the incident irradiances from the sun and earth. This temperature is modified from that which an ideal spherical sensor would attain by additional energy exchanges between the mirror and sensor and by the thermal lag of the sensor. The energy balance equation must be expanded to account for these terms.

The diagram in Figure 7 shows the energy flow paths that control the sensor's temperature. They are the absorbed irradiance streams from the sun and earth (1. 2. and 3.), the emittance of energy back to space (4. and 6.), the local radiant energy exchange between the mirror and sensor (5. and 7.), energy conducted along the post (8.), and the changes in the internal energy of the sensor itself. Since the post is physically small, its radiative energy transfer is assumed negligible.

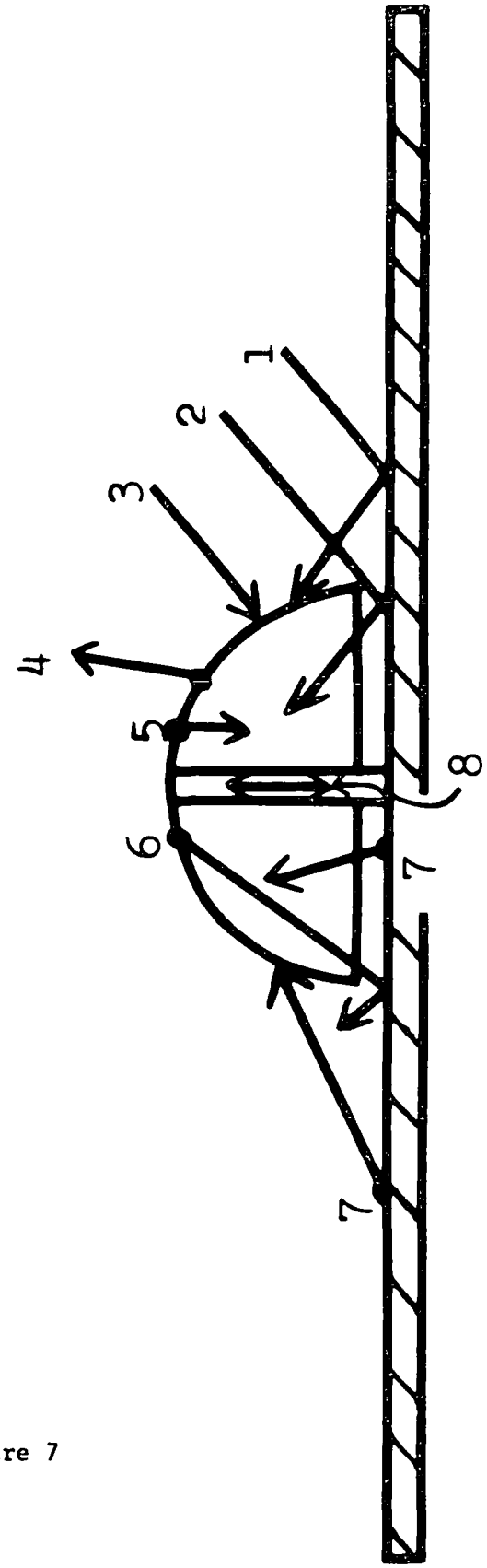

Energy Flows Controlling the Sensor's Temperature.

Figure 7

The energy balance equation for the spinning TIROS sensor is

$$\frac{\alpha_s}{\alpha_1}\ \frac{\pi}{2}\ R_s + \frac{\alpha_s}{\alpha_1}\ \frac{\beta}{2}\ R_r + \frac{\beta}{2}\ R_1 = 2\pi\ \frac{\mathcal{E}_1}{\alpha_1}\ \sigma\ T^4$$

$$- \frac{C_m}{2}\ \sigma\ T_m^4 + \frac{C_c}{2}\ (T - T_m) + \frac{C_t}{2}\ \frac{2\ (\sigma T^4)}{\partial t}\ , \quad (3.21)$$

where $C_m/2$ = is a lumped constant which includes the geometry and the emissivity of the mirror (ster).

$C_c/2$ = is a lumped constant which includes the conductivities and dimensions of the post's components, (ster-ly/min - deg.)

$C_t/2$ = is a lumped constant which includes the masses and the various heat capacities of the sensor's components (ster - sec).

T_m = mirror temperature (^oK).

As shown in Figure 6, the hemispheric sensor and mirror image appear as a full sphere. However, they absorb radiation from a point source as a sphere only half of the time, owing to the satellite's rotation. Therefore, the solid angles π and β on the left of (3.21) are divided by 2. On the other hand, the loss of energy through radiant emittance occurs over the hemisphere <u>all</u> the time. Thus a spinning mirror-backed hemisphere has essentially the same geometry as the ideal spherical sensor.

The terms on the right of (3.21) are the emittance of energy by the sensor to the mirror and to space, emittance of

energy by the mirror to the sensor, energy conduction along the post, and a correction for the sensor's thermal lag.

Temperature observations at the satellite are spaced 29.16 seconds apart. The thermal lag term is obtained, in practice, from two consecutive temperature observations T_1 and T_2. The mirror and sensor temperatures are averages during the same time interval, $\overline{T}_m$ and $\overline{T}$ respectively. Multiplying (3.21) through by 2, we have

$$\frac{\alpha_s}{\alpha_1} \pi R_s + \frac{\alpha_s}{\alpha_1} \beta R_r + \beta R_l = 4\pi \frac{\varepsilon_1}{\alpha_1} \sigma \overline{T}^4$$

$$- C_m \sigma \overline{T}_m^4 + C_c (\overline{T} - \overline{T}_m) + C_t (\sigma T_2^4 - \sigma T_1^4) \qquad (3.22)$$

This equation is similar to (2. 1) for the ideal spherical sensor with additional terms that account for mirror, post, and internal energy flows.

3.3 In-flight Determination of Equation Constants

Instruments on orbiting satellites may suffer in-flight degradation from their pre-launch calibration. For the black sensor on TIROS IV, the binder of the paint may evaporate, micro-meteorites may erode or even dent the sensor's surface, high energy particles from the sun may change the spectral properties of the paint, and the extreme temperature cycling of the

sensor during each orbit may flake the paint. Any of these possibilities can change the black sensor's pre-launch calibration. For example, the scanning radiometers of several TIROS meteorological satellites show marked changes in calibration after launch despite care in manufacturing. In-flight calibration in space is necessary to determine the equation constants and any instrumental changes.

In order to solve equation (3.22), it is necessary to determine the numerical value of the three constants C_t, C_m, and C_c which apply to the particular sensor in orbit.

Laboratory measurements by Sparkman (1964) show that C_m and C_c are related for a TIROS type hemispherical sensor, so that

$$C_m = k_1 C_c, \qquad (3.31)$$

where k_1 is a proportionality constant. It is not necessary to isolate these two constants since one can be expressed in terms of the other within the operating range of the sensor and mirror temperatures on the satellite. Thus only two constants C_c and C_t need be determined in equation (3.22).

We proceed as follows: When the satellite enters the shadow zone, the sensor undergoes a rapid change in temperature from values near $+20^{o}C$ to values near $-60^{o}C$ as shown in

Figure 8. We assume that the terrestrial radiation below the spacecraft is constant during the cooling interval even though this may not be the case. During the cooling interval, usually taken to be 6 readings or about 3 minutes time (450 miles of satellite travel), there is a large variation in the sensor and mirror temperature difference because during the same interval the mirror changes only a few degrees. A trial choice of C_t is made in (3.22), and different values of C_c are tried in a series of successive approximations adjusted so as to minimize the scatter of the calculated values of the earth's radiation below the spacecraft. This iteration technique converges rapidly.

The above procedure is repeated for many other cooling cases distributed within the precessional cycle of the satellite in order to remove any bias which might be introduced by the changing LWR from the earth over the 450 mile interval. Figure 9 shows the results of this procedure. The line of "best-fit" pairs of constants is based on the converged values of C_c for different choices of C_t, using 350 cooling cases for each pair of constants. Note that the range of possible thermal lag values is small for a large range of C_c values; thus the value of C_t is insensitive to the choice of C_c.

The straight line in Figure 9 establishes the relationship between C_t and C_c, so that C_t can be expressed as

$$C_t = k_2 C_c + k_3 , \qquad (3.32)$$

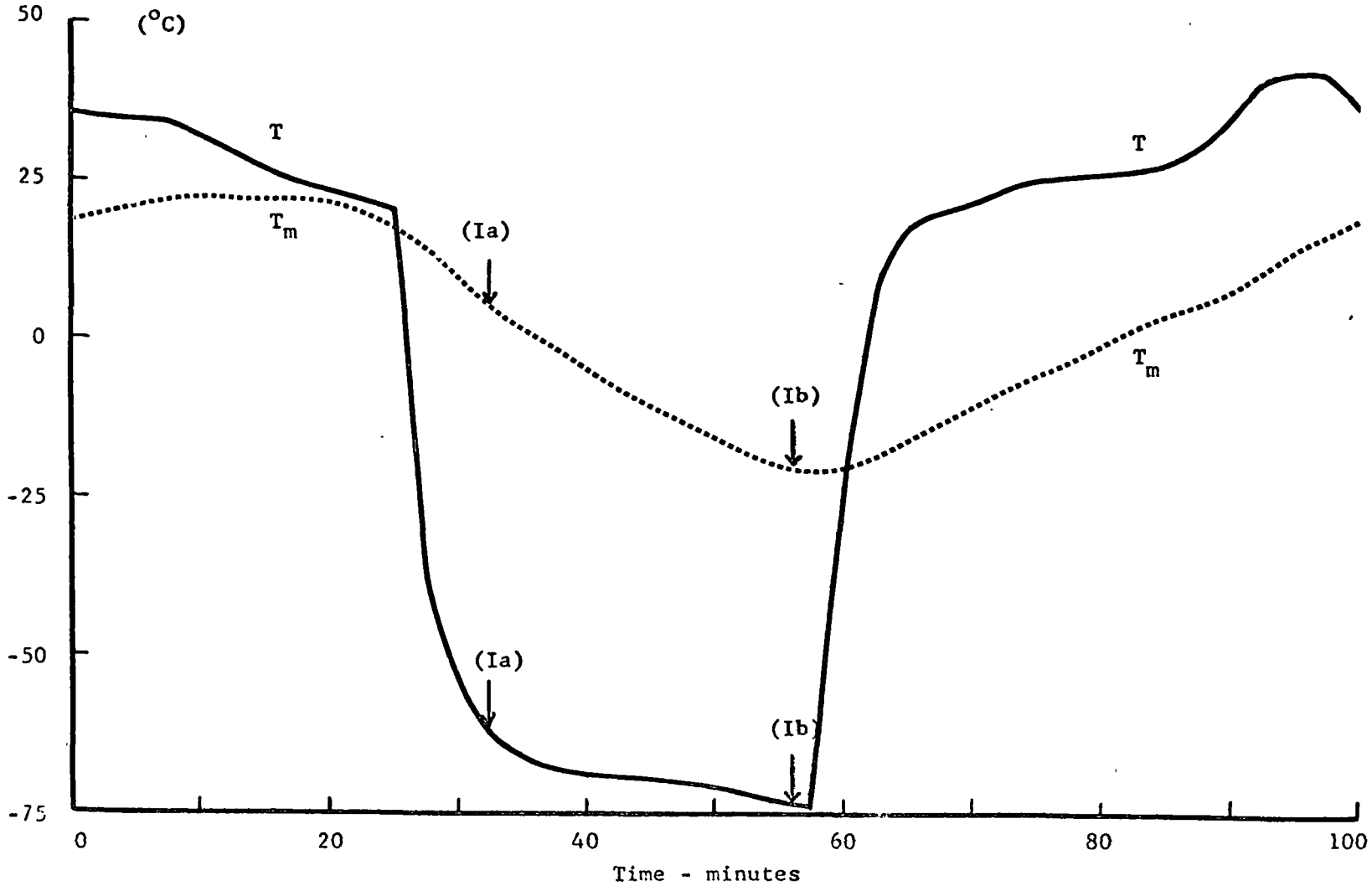

Figure 8 Typical Black Sensor and Mirror Temperature Observations During a TIROS IV Orbit

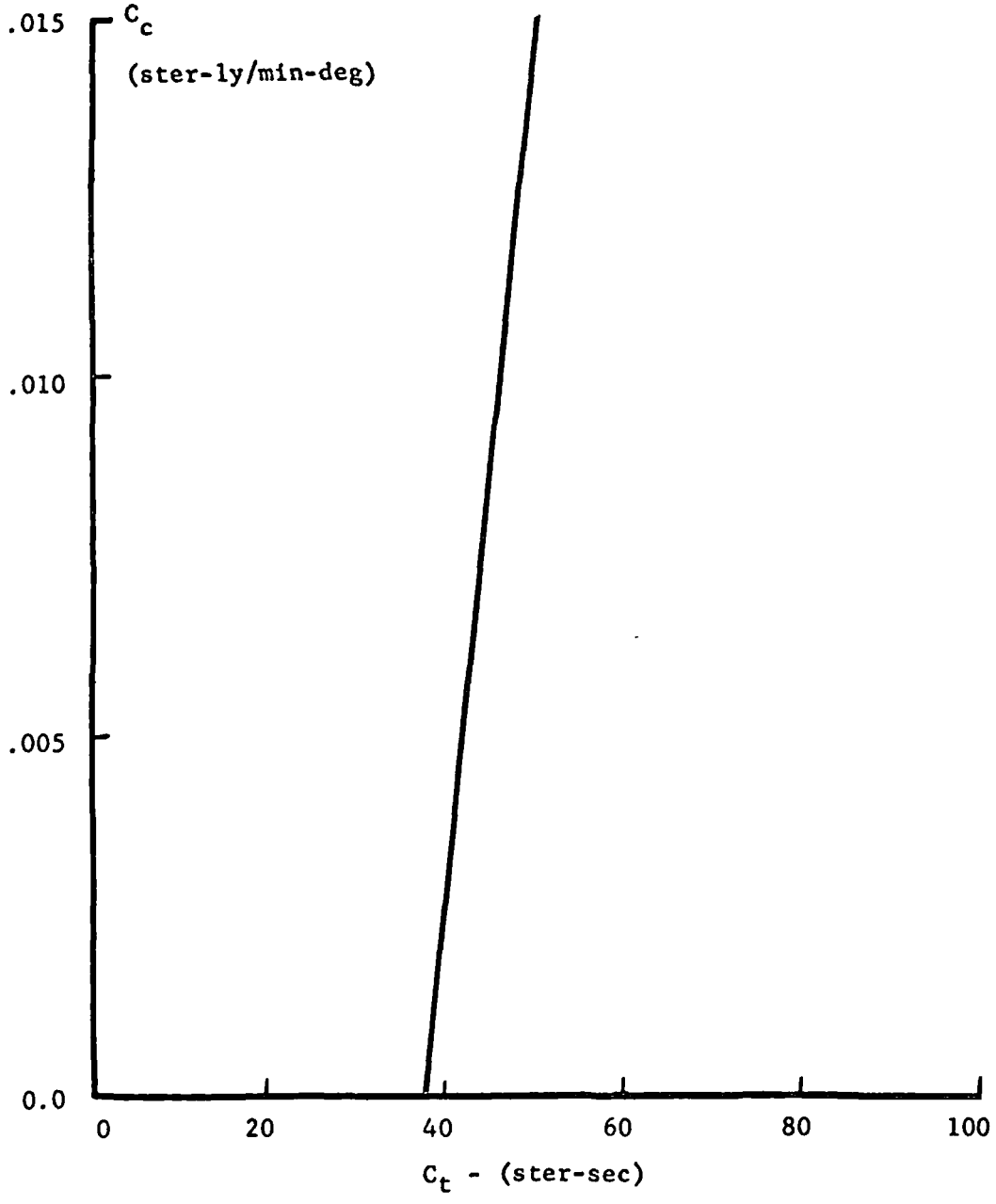

Figure 9 "Best-fit" Conduction and Thermal Lag Constants for the TIROS Black Sensor.

where k_2 is the slope of the line and k_3 is the zero intercept. Therefore, it is possible to write the nighttime form of the energy balance equation in terms of C_c using (3.31) and (3.32),

$$\beta R_1 = 4\pi \frac{\epsilon 1}{\alpha_1} \bar{T}^4 + C_c \left(- k_1 \sigma \bar{T}_m^4 + (\bar{T} - \bar{T}_m) \right.$$

$$\left. + k_2 (\sigma T_2^4 - \sigma T_1^4) \right) + k_3 (\sigma T_2^4 - \sigma T_1^4) \qquad (3.33)$$

The numerical value of C_c is determined from temperature data during the nighttime pass of the satellite. In Figure 8 the temperature of the mirror cools about 25°C between the beginning and end night positions, (Ia) and (Ib) on the graph, respectively. Corresponding to this mirror temperature decrease is a 12°C decrease in the sensor's temperature. In any one orbit of the satellite, the change in the sensor's temperature is due principally to the change in the mirror temperature and due to a small part on the difference in the LWR beneath the spacecraft between (Ia) and (Ib).

Our plan of attack is to take many temperature observations at positions (Ia) and (Ib) distributed within a precessional cycle of the satellite in order to remove any bias introduced by the changing LWR from the earth. These observations can be expressed as a summation of individual terms in (3.33) since

each term has units of energy. For position (Ia), subscript $_a$, we have

$$\sum (\beta R_1)_a = \sum(\text{1st term})_a + C_c \sum(\text{2nd term})_a + \sum(\text{3rd term})_a \qquad (3.34)$$

where the 1st, 2nd, and 3rd terms correspond symbolically to the three terms to the right of (3.33), respectively. Likewise, the summation for (Ib), subscript $_b$, is

$$\sum(\beta R_1)_b = \sum(\text{1st term})_b + C_c \sum(\text{2nd term})_b + \sum(\text{3rd term})_b \qquad (3.35)$$

We assume that $\sum(\beta R_1)_a$ is equal to $\sum(\beta R_1)_b$ for a precessional cycle. Therefore, it is possible to solve for the conduction constant C_c using (3.34) and (3.35).

$$C_c = \sum(\text{1st term})_a - \sum(\text{1st term})_b + \sum(\text{3rd term})_a - \sum(\text{3rd term})_b$$

all four summations divided by

$$\sum(\text{2nd term})_b - \sum(\text{2nd term})_a . \qquad (3.36)$$

The above procedure was used to determine the numerical value of C_c for the black sensor on TIROS IV. It was found

that C_c equals 0.010 ster-ly/min-deg.; from Figure 9, C_t equals 43.0 ster-sec.; and for a value of k_1 equal to 30 in (3.31), C_m equals 0.15 ster.

An additional check of the lag term is possible just after the spacecraft enters the earth's shadow (see the sharp drop in the sensor's temperature in Figure 8). At this position the sensor and mirror temperatures are nearly equal; thus the conduction term is zero and is neglected in the energy balance equation. Solving for C_t in (3.22), using the nighttime form of the equation, we have

$$C_t = \frac{4\pi \frac{\epsilon_1}{\alpha_1} \sigma \bar{T}^4 - \beta R_1 - C_m \sigma \bar{T}_m^4}{\sigma T_1^4 - \sigma T_2^4} \qquad (3.37)$$

To determine C_t in (3.37), we must assume a value for R_1. This assumption is not critical since the emission term $4\pi \frac{\epsilon_1}{\alpha_1} \sigma \bar{T}^4$ is six times greater than the magnitude of βR_1. Therefore, any error in our assumption of the LWR contributes a relatively small error in the computed value of C_t. For example, an error of $\pm$ 0.05 ly/min in R_1 leads to a $\mp$ 2.8 per cent error in the magnitude of C_t. The mirror radiation term in (3.37) is one order of magnitude smaller than βR_1 and is neglected.

Inspection of 50 cooling cases throughout the life of TIROS IV satellite indicates that the initial temperature drop after entering the shadow is about -18.5°C on the average. The sensor temperature $\overline{T}$ in (3.37) is roughly 288°K and taking β equal to 3.4 ster and R_1 equal to 0.33 ly/min, C_t is equal to 42.3 ster-sec, a magnitude in excellent agreement with the value of 43.0 ster-sec found previously. This additional check of C_t gives us greater confidence in the numerical values of the constants in the energy balance equation.

A reasonable error estimate of the constants in the equation is $\pm$ 5.0 per cent of their absolute magnitude. This error assessment agrees with laboratory measurements of a similar TIROS type hemispherical sensor tested by Sparkman (1964).

The discussion of this section shows that in-flight determination of the equation constants is possible using only the temperature measurements of the sensor and mirror in their space environment. This technique is a powerful tool to check the calibration of other instruments on the satellite as well as the black omni-directional sensor itself. The application of this in-flight calibration principle on future satellites might be considered.

3.4 Error Analysis of the TIROS IV Measurements

First let us consider the errors in the calculations using the energy balance equation (3.22). Four possible sources of error that could bias the computed magnitudes of the values are 1) errors in the sensor's emissivity, 2) errors in geometry and satellite orientation, 3) errors in the temperature calibration, and 4) errors in the values of the equation constants. Modifications to the energy balance equation are made to account for the first two of these errors. The last two are systematic errors in the measuring system and are treated quantitatively.

The sensor black paint departs from the ideal sensor in the long-wave region of the spectrum in that its spectral emissivity decreases with increasing wave length. From Wien's Law the wave length of maximum emission decreases as the temperature increases. As the maximum emission of the Planck function shifts to shorter wave lengths with increasing sensor temperature, the emissivity of the sensor's paint is more efficient and, therefore, increases with temperature.

Analysis of the spectral response of the black paint indicates that the emissivity varies 5 per cent within the operating range of the sensor's temperature. To compensate for this error in (3.22), the scaling ratio $\frac{\mathcal{E}_1(\bar{T})}{\alpha_1(250^\circ K)}$ replaces the ratio $\frac{\mathcal{E}_1}{\alpha_1}$, where the emissivity is a function of the sensor's temperature $\bar{T}$ based on the spectral response of the black paint.

The absorption cross section (solid angle β) of the black hemisphere can vary with earth-satellite orientation. Two factors contributing to this error are the crack under the sensor in Figure 6 and the imperfect reflection of the mirror's surface. Radiant energy can be trapped under the sensor as shown by component 6 in Figure 7. For a spinning sensor, the amount of energy absorbed in this manner varies with orientation of the incoming stream to the spin axis of the satellite. The effect of this error increases β. Compensating toward lower values of β is the radiant stream 1 in Figure 7 which is partially absorbed by the mirror before reaching the sensor. Investigation of these factors based on sensor geometry and a reasonable absorptivity for the mirror's surface shows that β varies about 0.1 steradian with earth-satellite orientation. This variation, about 3 per cent, is included in the calculations.

The accuracy of the calculations using (3.22) depends principally on the known values of the constants in the equation and to a small degree on the absolute accuracy of the temperature measurements. The magnitude of the maximum error is determined below based on the $\pm$ 5 per cent accuracy of the equation constants from the previous section and on the $\pm$ .15 ^{o}K uncertainty in the sensor's temperature due to quantization of the satellite's signal during data processing.

The constants in (3.22) with indicated accuracy of $\pm$ 5 per cent, are

$$C_m = 0.300 \pm .015 \text{ (ster)},$$

$$C_c = 0.0100 \pm .0005 \text{ (ster ly min}^{-1} \text{ deg}^{-1} \text{)},$$

$$C_t = 43.0 \pm 2.15 \text{ (ster min)}.$$

It is convenient when assessing the errors to consider day and night calculations separately. The following data are typical observations:

Table 1

TYPICAL SATELLITE OBSERVATIONS FOR DAY AND NIGHT MODES

Data	Day	Night
$\bar{T}$	300 °K	210 °K
$\bar{T}_m$	265 °K	265 °K
$(\bar{T}-\bar{T}_m)$	35 °C	-55 °C
$(\sigma T_2^4 - \sigma T_1^4)$	.0026 ly/min	.0009 ly/min

The computed magnitudes of the maximum absolute errors for each term to the right of (3.22) are shown in Table 2 (units in ster-ly/min).

Now let us consider the error analysis of the actual LWR, albedo, and net radiation calculations based on the maximum absolute errors of the energy balance equation.

Table 2

SYSTEMATIC ERROR FOR EACH TERM IN THE ENERGY BALANCE EQUATION

Error	Day	Night
Sensor Emittance	.017	.008
Mirror Radiation	.007	.007
Post Conduction	.018	.028
Thermal Lag	.006	.002
Maximum Absolute Error	0.048	0.045

The maximum absolute error for nighttime calculations is .045 ster-ly/min, an uncertainty of $\pm$ 3.5 per cent in the computed values. It is reasonable to assume an additional uncertainty of $\pm$ 1 per cent in the known solid angle β which leads to a total uncertainty of $\pm$ 4.5 per cent in LWR averages, about $\pm$ .015 ly/min.

The absolute error in the albedo calculations, $d\bar{A}$, is determined in a similar manner as in equation (2.53) assuming in the worst case that dX and dY in Table 2 are opposite in sign, .048 and -.045 respectively.

$$d\bar{A} = 100 \ \frac{.048 \ (\ 4.70 - 2.80 + 1.20 \ ) + 4.70 \times .045}{22.1}$$

$$= 1.6\,\%.$$

The albedo error will vary with latitude since Y in (2.52), the LWR term, is a function of latitude. An empirical formula to compute absolute albedo error from (2.54), based on the absolute magnitude of the albedo, was apparent after analysing calculated albedo errors for all latitudes: Albedo error $\lesssim^{+}_{-} 0.055\bar{A}$ (indicating an absolute error in albedo %). This says that the maximum error for a 45% albedo is $^{+}_{-}$ 2.5%, for 35% - $^{+}_{-}$ 1.9%, and for 25% - $^{+}_{-}$ 1.4%. It is important to remember that this error acts in the same direction for all albedo values. The curves for the meridional variation of albedo in Figure 11 will be shifted up or down, depending on the sign of the error, and the shift will be greater for higher values than for lower values.

The accuracy of the albedo averages also rests on the initial assumption that day and night averages of LWR are equal. Astling and Horn (1964) investigated the diurnal variation of LWR using TIROS II scanning radiometer data. Their results indicate a .01 to .02 ly/min increase during the day. On the other hand, Bandeen, et. al. (1964) show results based on TIROS VII data for the equatorial Pacific Ocean that indicate a decrease during the day. This possible contradiction may be explained by a systematic bias introduced into the data by each satellite. At any rate, the error introduced by the assumption of day-night equality of LWR averages is probably no greater

than the uncertainty in night LWR averages themselves, of $\pm$ .015 ly/min. Therefore, the uncertainties in the albedo averages stated above are still reasonable.

The equation to compute the mean net radiation (2.47), written in symbolic notation of (2.52), is

$$\overline{RN}_t = \left(1 - \frac{X - Y}{Z} \right) \bar{R}_s - \frac{Y}{\beta} . \qquad (3.41)$$

Differentiating and simplifying as in (2.54), we have

$$dRN_t = - \bar{R}_s \left(\frac{-dX\,(Z - X + Y) + Z\,dY}{Z^2} \right) - \frac{dY}{\beta} . \qquad (3.42)$$

Typical values for $\bar{R}_s$ and β are 0.5 ly/min and 3.4 ster, respectively. Substituting in (3.42), we have

$$d\overline{RN}_t = -0.5 \left(.016 \right) + \frac{.045}{3.4}$$

$$= .005 \text{ ly/min.}$$

The calculation shows how the error in the difference of values is less than the error in each value. The differential $d\overline{RN}_t$ increases as $\bar{R}_s$ becomes smaller. The smallest value of $\bar{R}_s$ considered in this study is .215 ly/min , which, in the worst case, leads to the error in net radiation of .010 ly/min.

One aspect in the accuracy of measurements using a spherical sensor that has not been mentioned before is limb-darkening to LWR and limb-brightening to reflected SWR. These two effects

are evident from channel 2 and 3 scanning radiometer measurements on TIROS IV satellite, respectively. A spherical sensor gives equal weighting to radiation streams from all directions whereas a flat sensor weights radiation streams as a cosine function of the angle to the normal of the surface. As a result, a sphere measures slightly higher values of albedo and lower values of LWR than a flat sensor would measure under the same circumstances.

Bignell (1962) states that in unusual and extreme meteorological conditions, the limb-darkening and limb-brightening errors for individual measurements might reach $\pm$ 2 per cent and $\pm$ 10 per cent respectively. These errors would be much less for average values of LWR and albedo. Calculations using the mean limb-darkening curve of Wark, et. al. (1962) indicate that the mean error in using a spherical sensor as compared to a flat sensor is less than one half of one percent, about .0017 ly/min, for typical values of LWR from the earth. The error due to limb-brightening is probably on the order of 1 to 2 per cent of the albedo value. These errors are quite small and can be neglected in the calculations.

IV. SUMMARY OF TIROS IV MEASUREMENTS

In previous sections we are concerned with the techniques used to obtain useful values from the signals telemetered by the TIROS IV satellite. In this section we are concerned with the global summary of these measurements.

The TIROS IV measurements include four months of usable data for the period February 8 to June 11, 1962, gathered from seventy-five per cent of the earth's area. The averaging periods used in this study for nearly two precessional cycles include the periods February 8 through April 10 and April 11 through June 10. While the satellite completes more than 14 orbits in a 24 hour period, only five to six orbits are available per day on the average. This limitation was caused by the lack of additional data acquisition stations. Further details concerning the areal sampling, the available orbits, and the orbital parameters of TIROS IV are presented by NASA Staff Members (1963).

4.1 Comparison of Measurements for Two Precessional Cycles

Figure 10 shows the meridional variations of LWR. The curves for both periods indicate lower values at tropical latitudes, maximum values at subtropical latitudes, and decreasing values poleward. These features are associated with the cloud

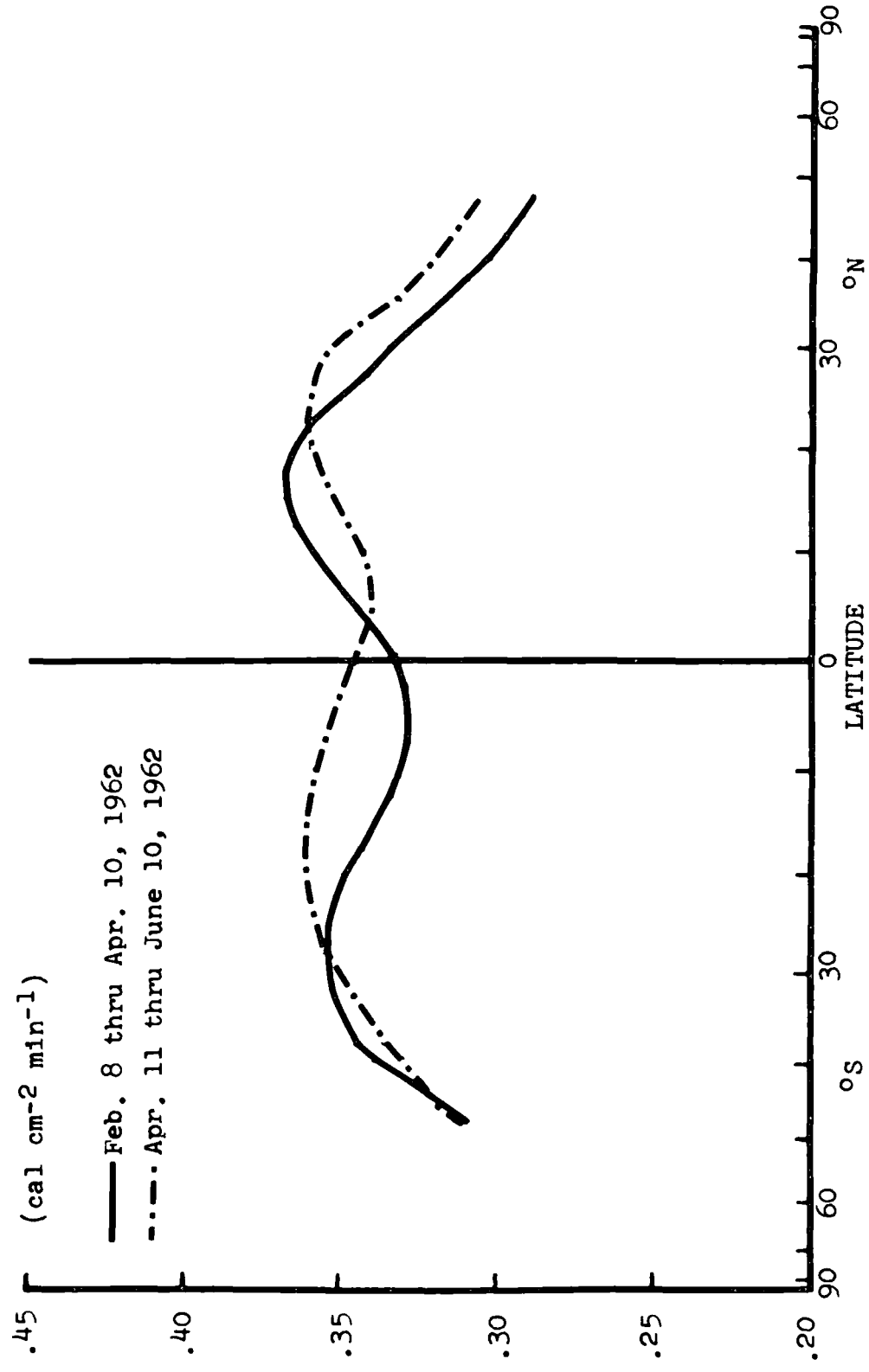

Comparison of the Meridional Variation of Long-wave Radiation for two Precessional Cycles.

Figure 10

and moisture distribution within the ITC, the subtropical highs and colder regions at higher latitudes.

The equatorial minimum in outgoing radiation, associated with the deep moisture layer of the ITC, crosses the equator during the time between the two periods and apparently the ITC has a deeper layer of moisture during the late summer (in the southern hemisphere) as indicated by the lower minimum of LWR.

Both maxima associated with the subtropical high belt move northward during the period. However, the maxima of LWR in the northern hemisphere decreases while the southern hemisphere maxima increases slightly. This observation implies that the winter subtropical high is a region of maximum heat loss. A possible explanation is that the moisture layer at these latitudes during winter is at a minimum. An inspection of London's (1957) climatological data for the seasons verifies this point, and his data indicate a minimum total optical depth of water vapor during the winter season. A dry atmosphere over a relatively warm surface results in large values of radiative loss, in agreement with calculations and verified by radiometersonde measurements.

The increase in outgoing LWR at middle latitudes is greater in the northern hemisphere than the decrease in the southern hemisphere. The difference in the area of land masses between the two hemispheres could explain this effect. Continental

climates show larger seasonal variations of temperature and moisture than do maritime climates. Consequently, the larger change in LWR occurs in the northern hemisphere, an area including the continents of Asia and North America, rather than in the southern hemisphere, an area dominated by oceans.

The meridional profiles of albedo in Figure 11 show slight maxima at the ITC, minima in the subtropical regions, and increasing values poleward again in agreement with what we would expect from climatology. In the second period, there is a one to three per cent increase in albedo at the subtropical latitudes in both hemispheres.

The profiles of net radiation in Figure 12 show a movement of maximum values northward, in phase with the subpolar point shown in Figure 4. The decrease in values during the second period is associated with the albedo increase and the diminishing incident solar radiation. Since the net radiation is the primary forcing function of the atmospheric circulation, it is evident that these changes can have a profound effect on global weather.

4.2 Comparison of TIROS IV Measurements with Previous Estimates

London has presented his seasonal estimates of the global radiation budget of the earth for the northern hemisphere. His estimates for the fall and spring seasons can be compared with

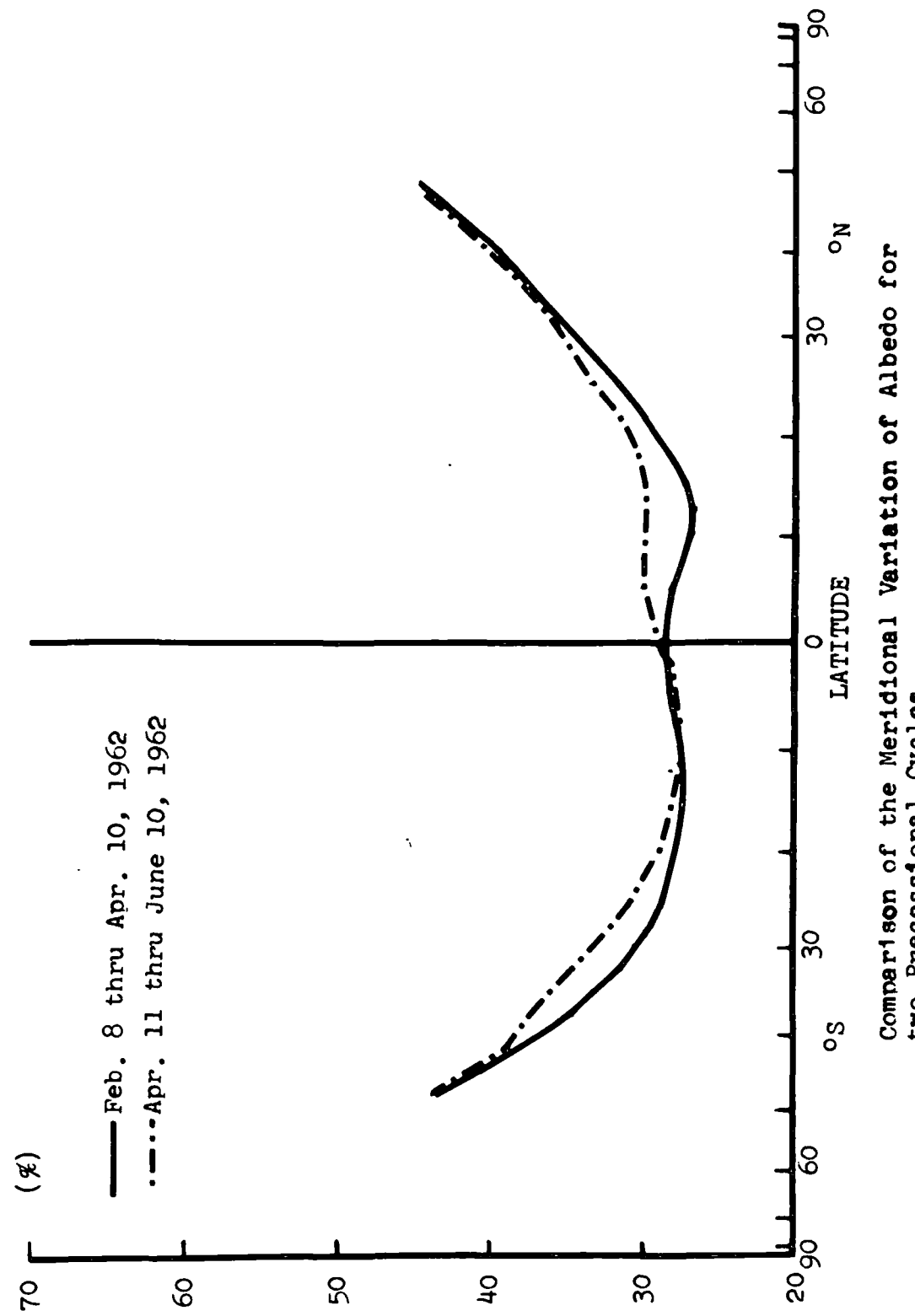

Comparison of the Meridional Variation of Albedo for two Precessional Cycles.

Figure 11

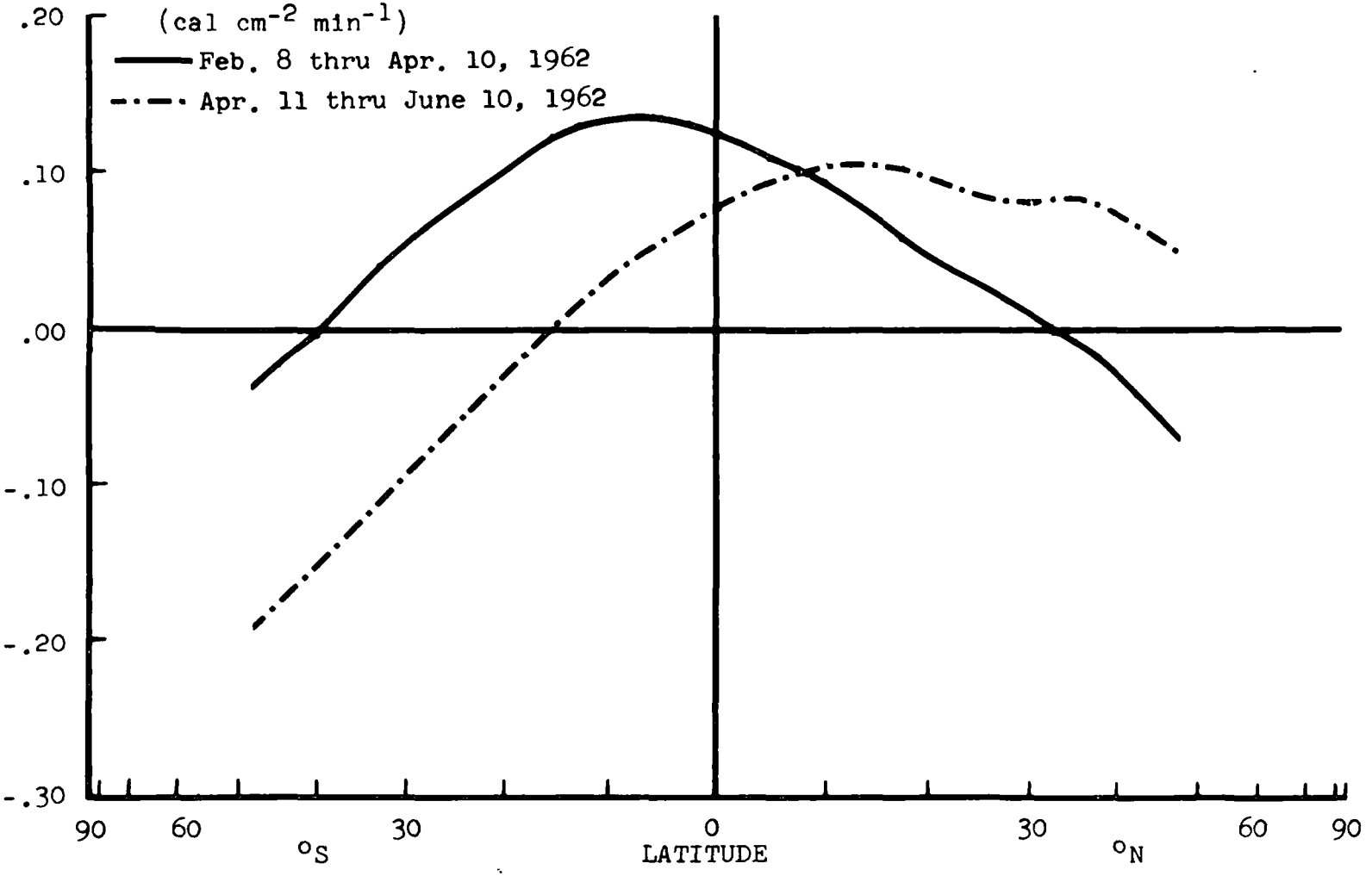

Figure 17

Comparison of the Meridional Variation of Net Radiation for two Precessional Cycles.

satellite observations for March, April, and May. The stippled lines in Figures 13 and 14 indicate the uncertainty in the values based on the discussion of Section 3.4.

Figure 13 shows a comparison of London's values with LWR measurements from the satellite. The agreement of his values with the measurements is excellent in the northern hemisphere. However, in the southern hemisphere, the satellite observations at middle latitudes are slightly higher than those of London. In this comparison we are using calculations for the northern hemisphere and comparing them to observations in the southern hemisphere. One can argue that the satellite observations should be higher because of the lag in the seasons for ocean areas. Since the southern hemisphere is predominantly an ocean area as compared to the northern hemisphere, we can expect warmer temperatures and consequently a greater LWR loss to space.

Similarly, the comparison of the meridional profile of albedo is shown in Figure 14. The satellite observations indicate a lower albedo in tropical latitudes of four to six per cent and higher values of three to five per cent in middle latitudes. Since the sun angle in the tropics is high and the surface area is relatively large, this decrease in albedo at these low latitudes indicates a greater absorption of energy than indicated by London's values.

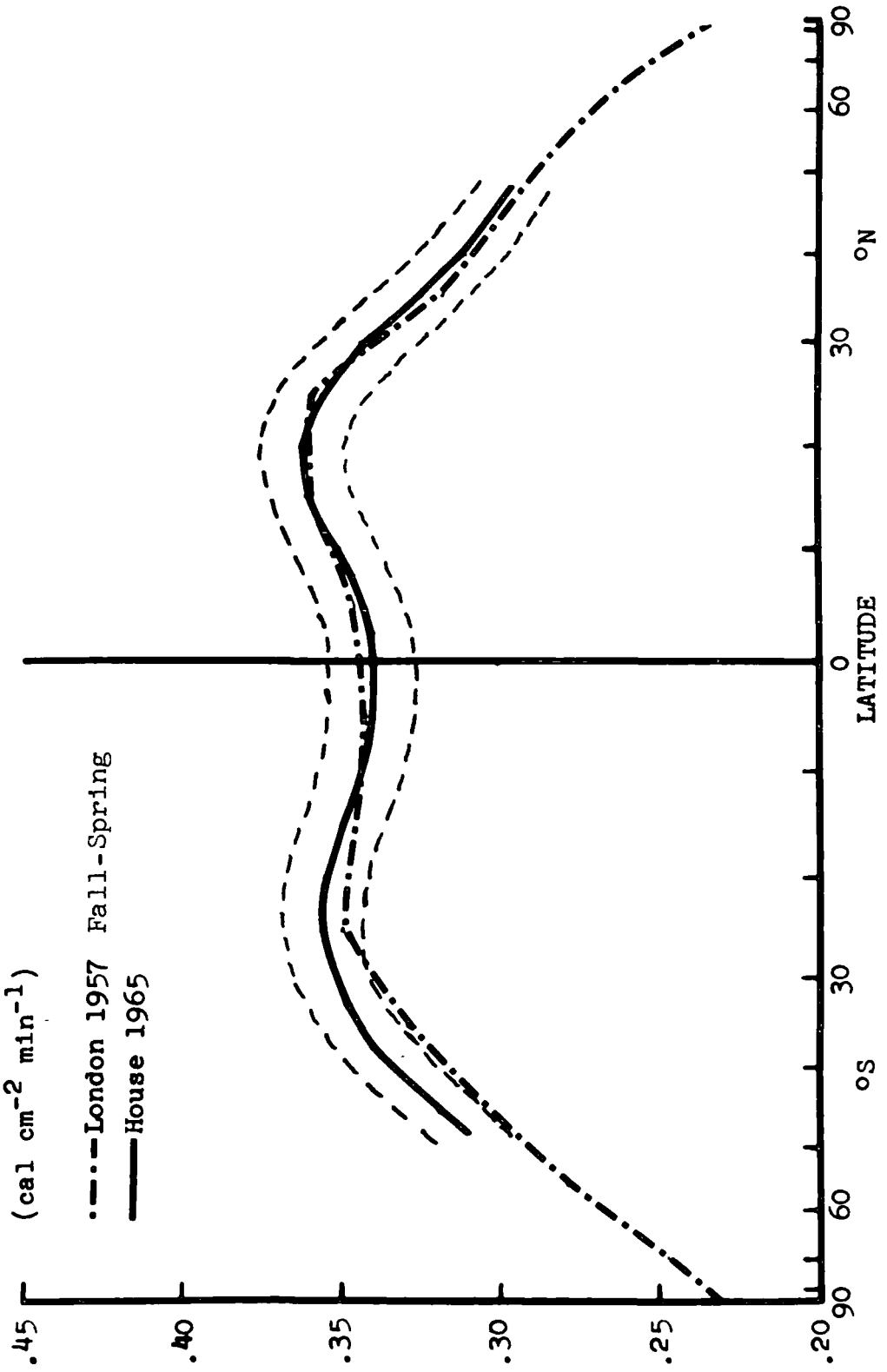

Comparison of the Meridional Variation of Long-wave Radiation for March, April, and May.

Figure 13

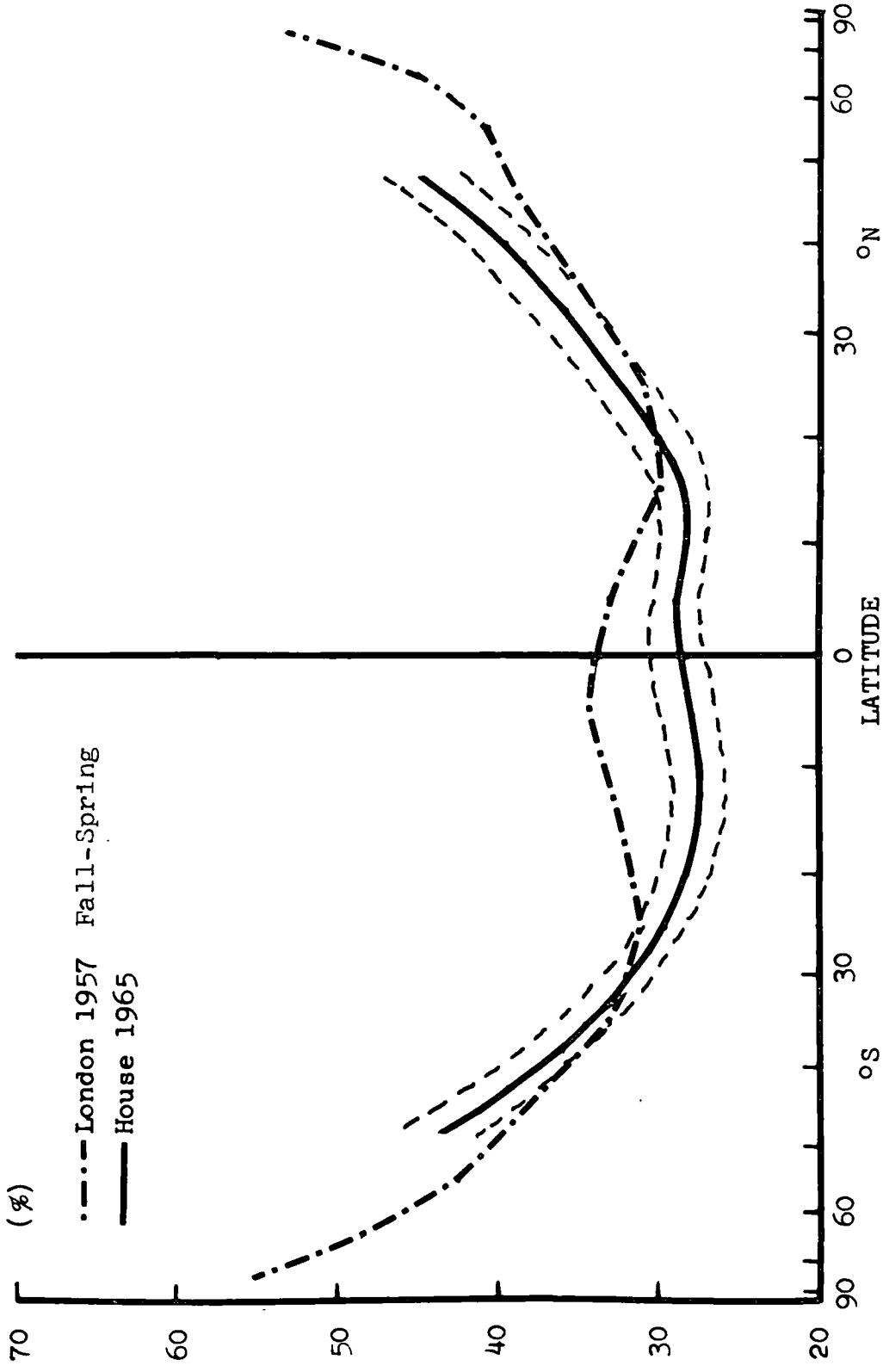

Comparison of the Meridional Variation of Albedo for March, April, and May.

Figure 14

In Figure 15 the meridional profiles of net radiation from TIROS IV are compared with the profiles given by Simpson (1928) and London (1957). The TIROS IV measurements indicate higher values in tropical latitudes and slightly lower values in middle latitudes. Even though Simpson's calculations of the individual components of absorbed and emitted radiation have been shown to be in error, his estimate of net radiation proved to be quite accurate.

We can investigate the possibility of global radiative equilibrium for the three month period based on the variation of net radiation in Figure 15. Unfortunately, satellite measurements for the two polar areas are missing. However, a reasonable extrapolation of the net radiation profile can be made to a value of -.20 ly/min at the south pole, based on average radiometersonde measurements (White, 1963), and to a value of -.11 ly/min at the north pole, based on the mean value of London and Houghton. Within the error uncertainty of the net radiation measurements of $\pm$ .005 ly/min, the earth-atmospheric system is in radiative equilibrium for the three month period of observation. This conclusion implies that the global rates of heat storage are in balance, even during the period of observation where the seasonal transitions between winter and summer are at a maximum.

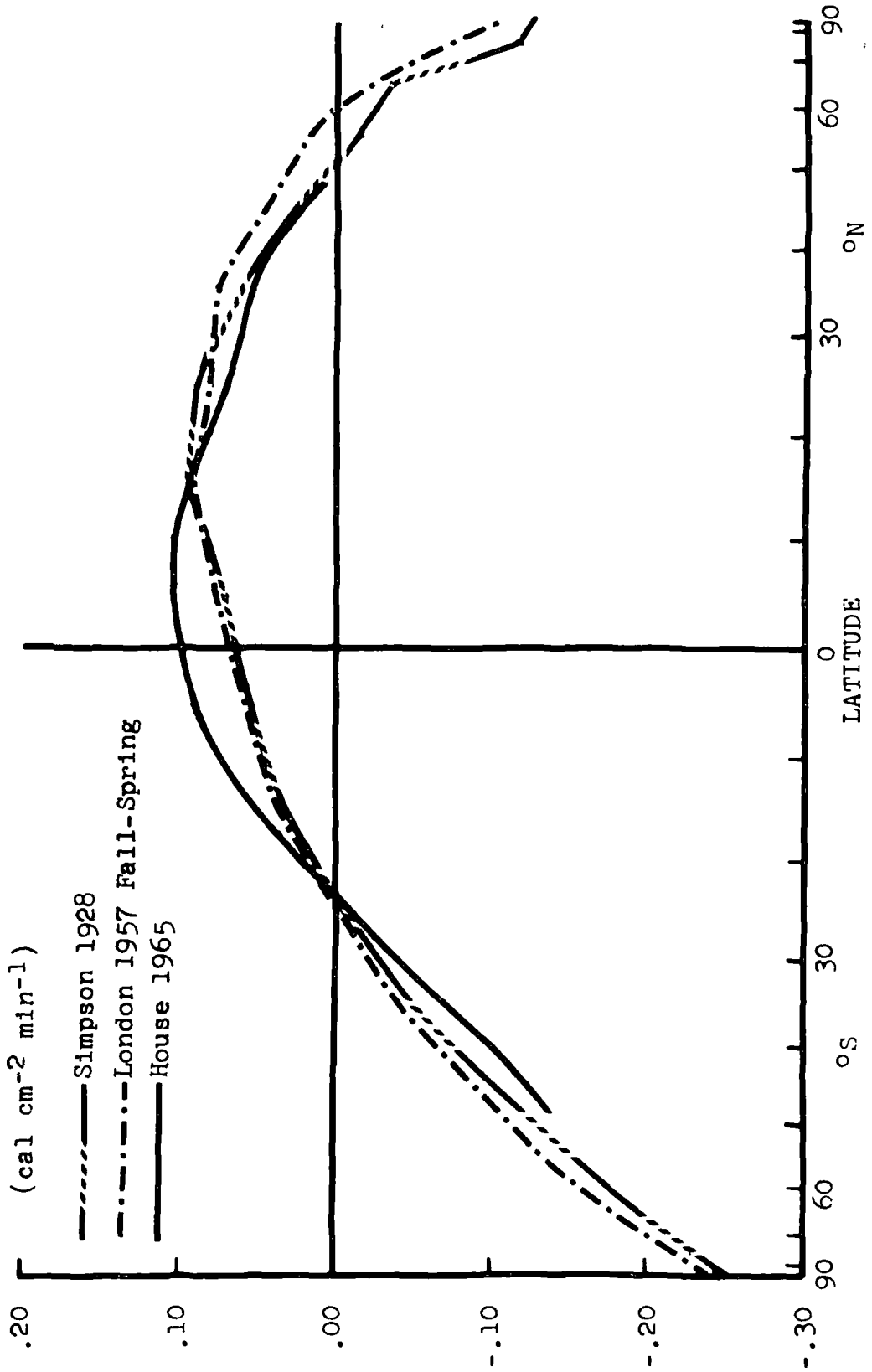

Comparison of the Meridional Variation of Net Radiation for March, April, and May.

Figure 15

4.3 Radiation Balance of the Earth

In previous studies scientists have determined the planetary heat transport of the atmosphere and oceans by calculating the mean annual meridional profiles of net radiation from climatological summaries of temperature, moisture, and cloud distributions. One of the first studies was the work of Simpson (1928, 1929) followed later by Baur and Philipps (1934, 1935), Houghton (1954), Lettau (1954), and London (1957). In this chapter the planetary heat transport will be determined by the same method. However, actual satellite measurements of net radiation will be used in lieu of indirect calculations.

When considered jointly, the data from both hemispheres represents eight months of observations from an annual cycle of one combined hemisphere. One may note that the spring and fall data include the important periods of the transition seasons. The gaps in an annual sample are the periods of the winter and summer seasons, representing a time when gross planetary circulation features are in a semi-steady state condition. On this basis the satellite observations are averaged from both hemispheres of the earth to study the planetary transport of heat for a mean hemisphere.

4.31 Heat Transport Calculation

On the planet earth the long-time annual mean temperature of the atmosphere is observed to be nearly constant. In order to maintain temperature equilibrium, an addition of energy at tropical latitudes requires the transport of heat poleward by the oceans and the general circulation of the atmosphere to the heat sink at higher latitudes. Thus, the positive net radiation values observed at tropical latitudes and the negative values at polar latitudes determine the poleward heat transport.

The total heat added within a zonal ring is given by the product of the net radiation and the area of the zone. The transport of heat, PT_i, across the poleward boundary of the i^{th} zonal ring (i = 1, m) is

$$PT_i = \sum_{i=1}^{m} (RN_t \times A_z)_i \qquad (4.311)$$

where A_{zi} is the area of the i^{th} zone.

In the transport calculation a small systematic error in the value of the net radiation may lead to a large error in the magnitude of the energy transport. A positive error in net radiation causes an over-estimate for the heat transport while a negative error produces an under-estimate. In Section 3.4 it was stated that the absolute error of the net radiation values is .005 ly/min. If this error exists, the magnitude of the

maximum heat transport will be in error by ten per cent and the latitude of maximum transport will be displaced one and one-half degrees from its true position. Therefore, the uncertainty in the magnitude of maximum heat transport, based on the maximum possible systematic error in the measurements, is $\pm$ 0.8×10^{16} cal/min, and the corresponding latitude displacement error is $\pm$ 1.5°.

4.32 Comparison of the Observed Heat Transport with Previous Estimates

Figure 16 shows a comparison of the annual LWR values given by Houghton and London with satellite measurements for a mean hemisphere. The dashed line is an extrapolation of the observations to the poles based on averages by London and Houghton. The agreement between satellite observations and London's values is remarkable. The difference is never greater than .01 ly/min.

In Figure 17 a similar comparison of the albedo profiles is presented. The satellite profile is extrapolated linearly to an albedo of 61 per cent at the pole. There are significant differences between the calculated and observed results. Observations indicate lower albedos of 3 to 5 per cent equatorward from latitude 20° and higher values of 5 to 8 per cent poleward from latitude 25°, about a 15 per cent decrease and increase, respectively, of the absolute magnitude of albedo values.

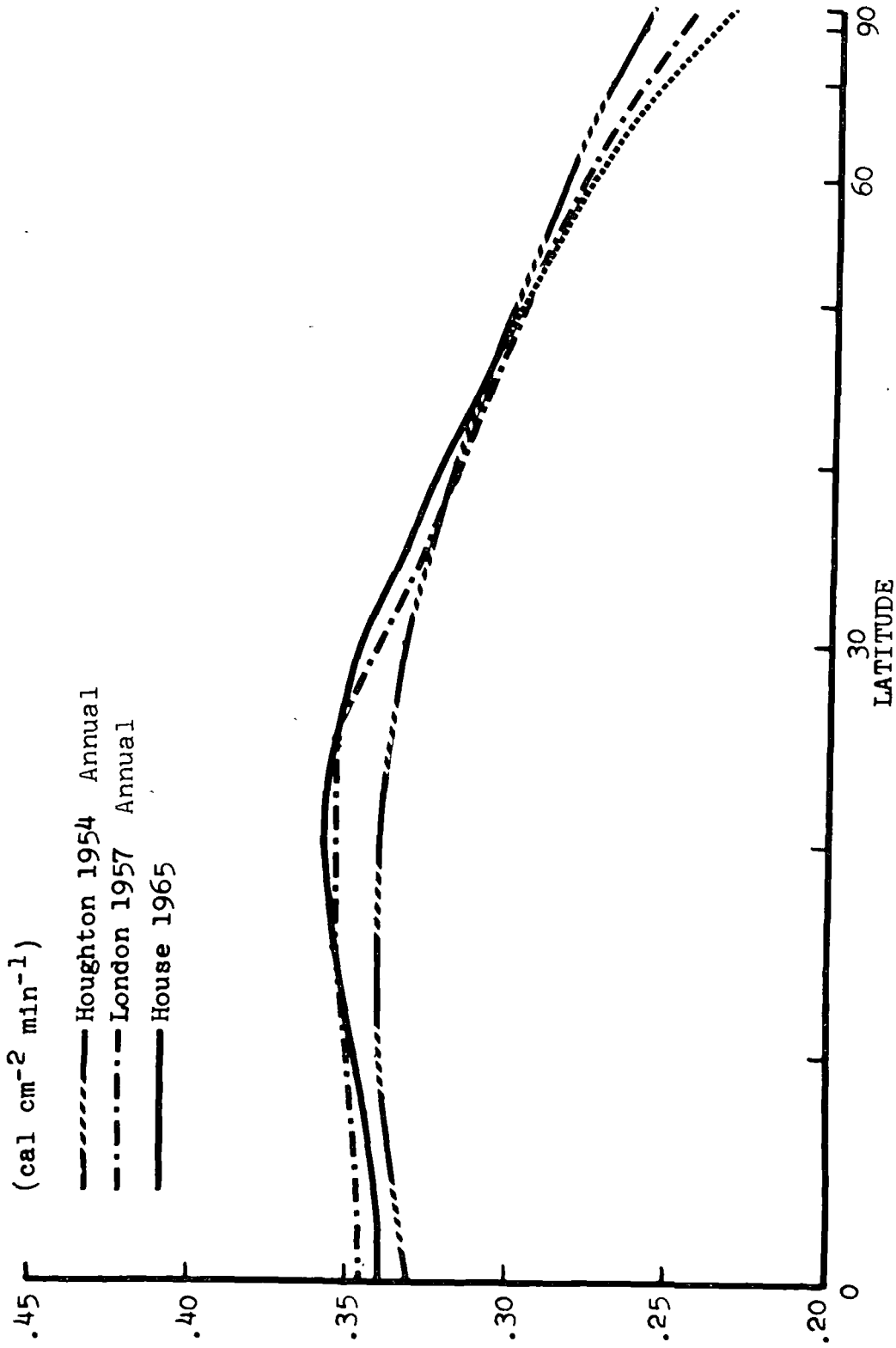

Figure 16

Comparison of the Annual Meridional Variations of Long-wave Radiation.

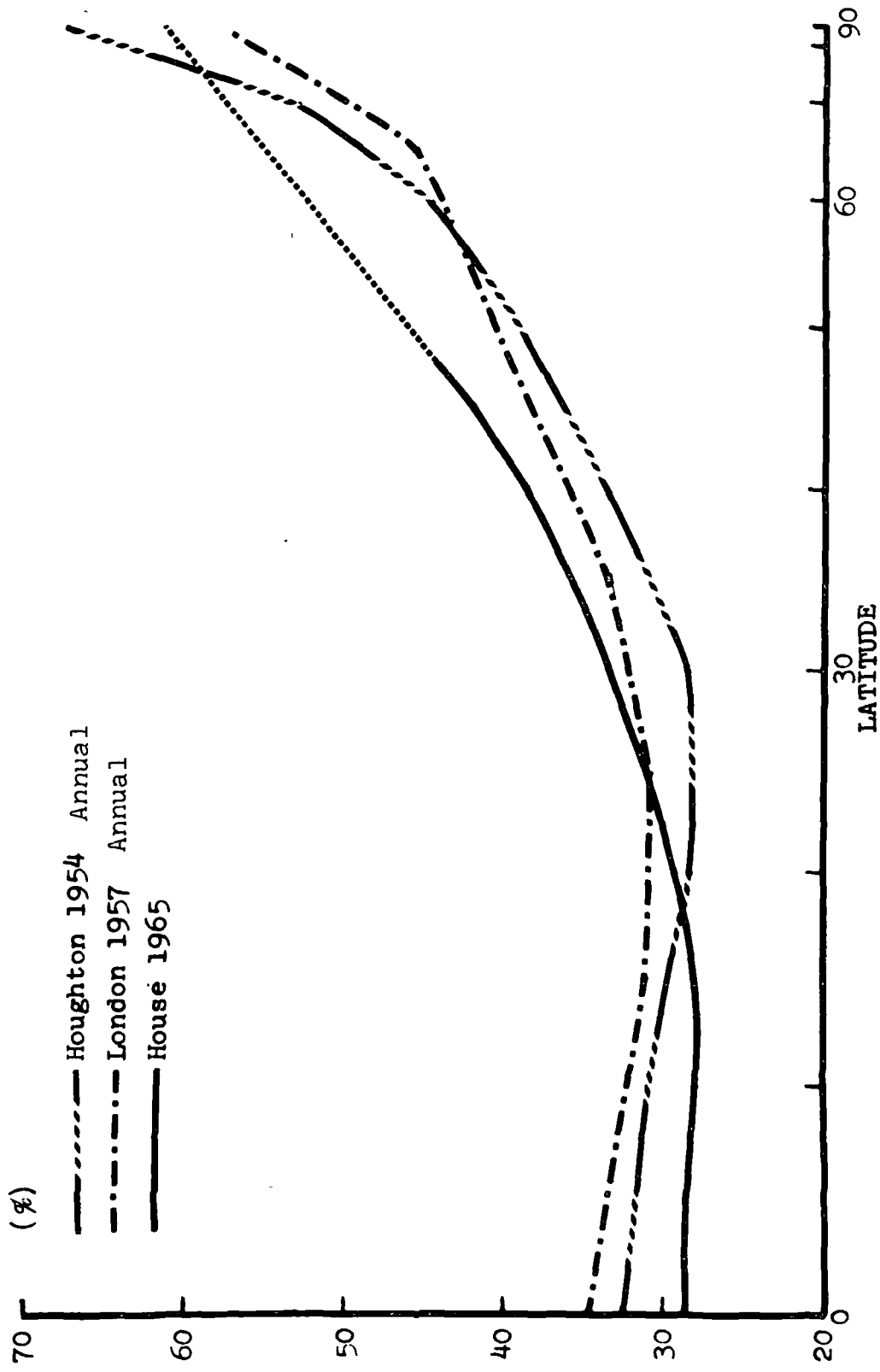

Comparison of the Annual Meridional Variations of Albedo.

Figure 17

The computed global albedo is 35 per cent, based on a weighted mean for the incoming solar energy using the albedo measurements in Figure 17. This value is in good agreement with the estimates of 35 per cent by Fritz (1949) and 35.2 per cent by London. In the comparison of Figure 15, a lower observed albedo implies a greater amount of absorbed energy by the earth-atmosphere system; conversely, a higher albedo implies a smaller amount of absorbed energy. The satellite observations indicate a greater input of energy at low latitudes and a smaller input at higher latitudes than the profiles of Houghton and London. Since the LWR variation in Figure 16 is virtually the same, the results indicate a greater radiative source of heat at tropical latitudes and a greater sink of heat at higher latitudes.

The mean hemisphere radiation balance of the earth in Figure 18 is determined from the satellite profiles in Figures 16 and 17. The latitude of radiation balance, 33.5°, is given by the intersection of the curves of absorbed and emitted radiant flux densities. The area between the curves to the left of the intersection is a measure of the heat source, and the area to the right, the heat sink.

The poleward flux of heat required to maintain the radiation balance using (4.311) is computed from Figure 18. Figure 19 shows a comparison of the planetary heat transport values with calculations by London and Houghton. The agreement is quite

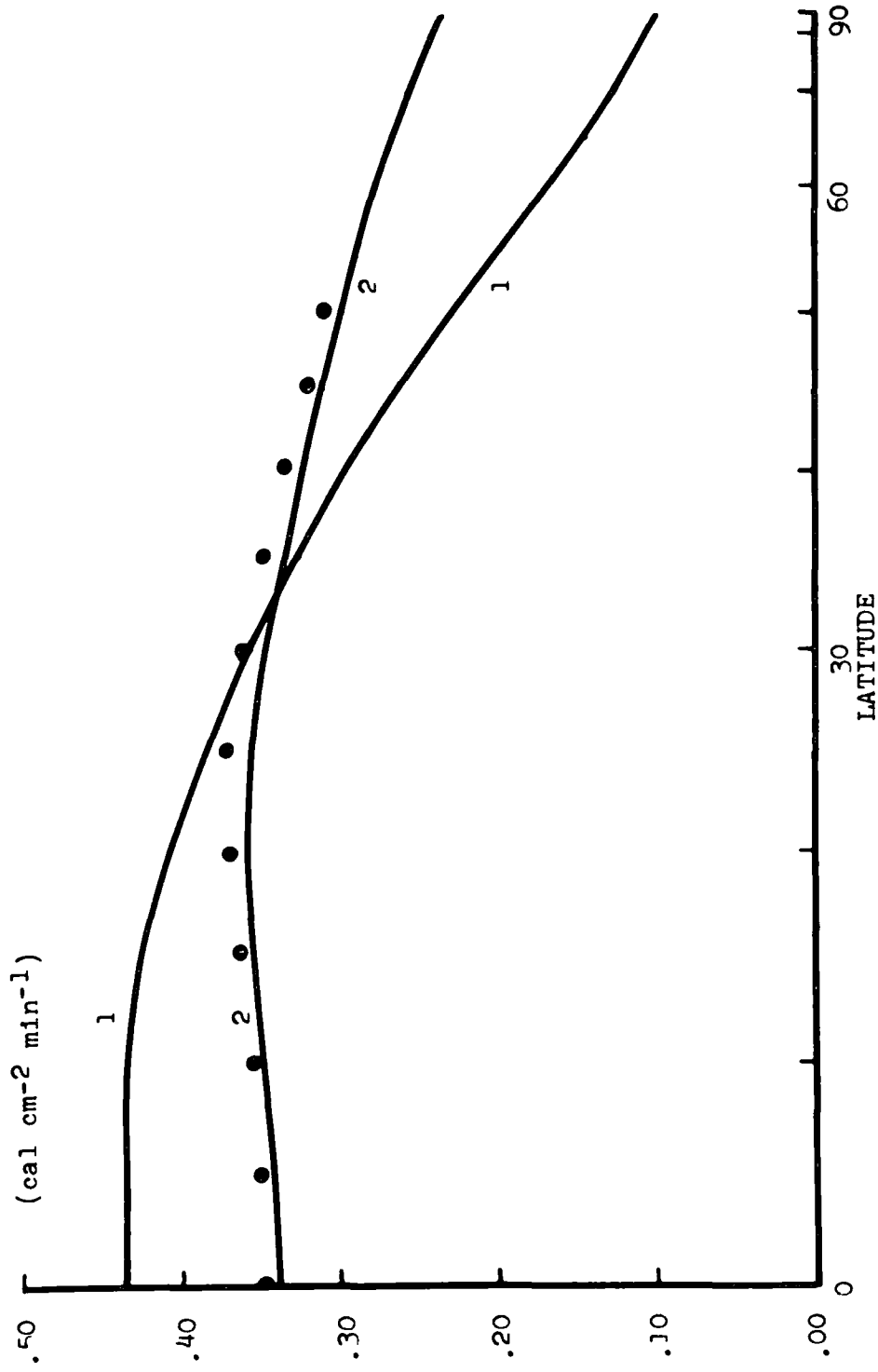

Figure 18

The Mean Radiation Balance of the Earth from TIROS IV Satellite:
Curve 1 - Absorbed Short-wave Radiation.
Curve 2 - Emitted Long-wave Radiation.
Dots - EXPLORER VII Mean Long-wave Radiation.

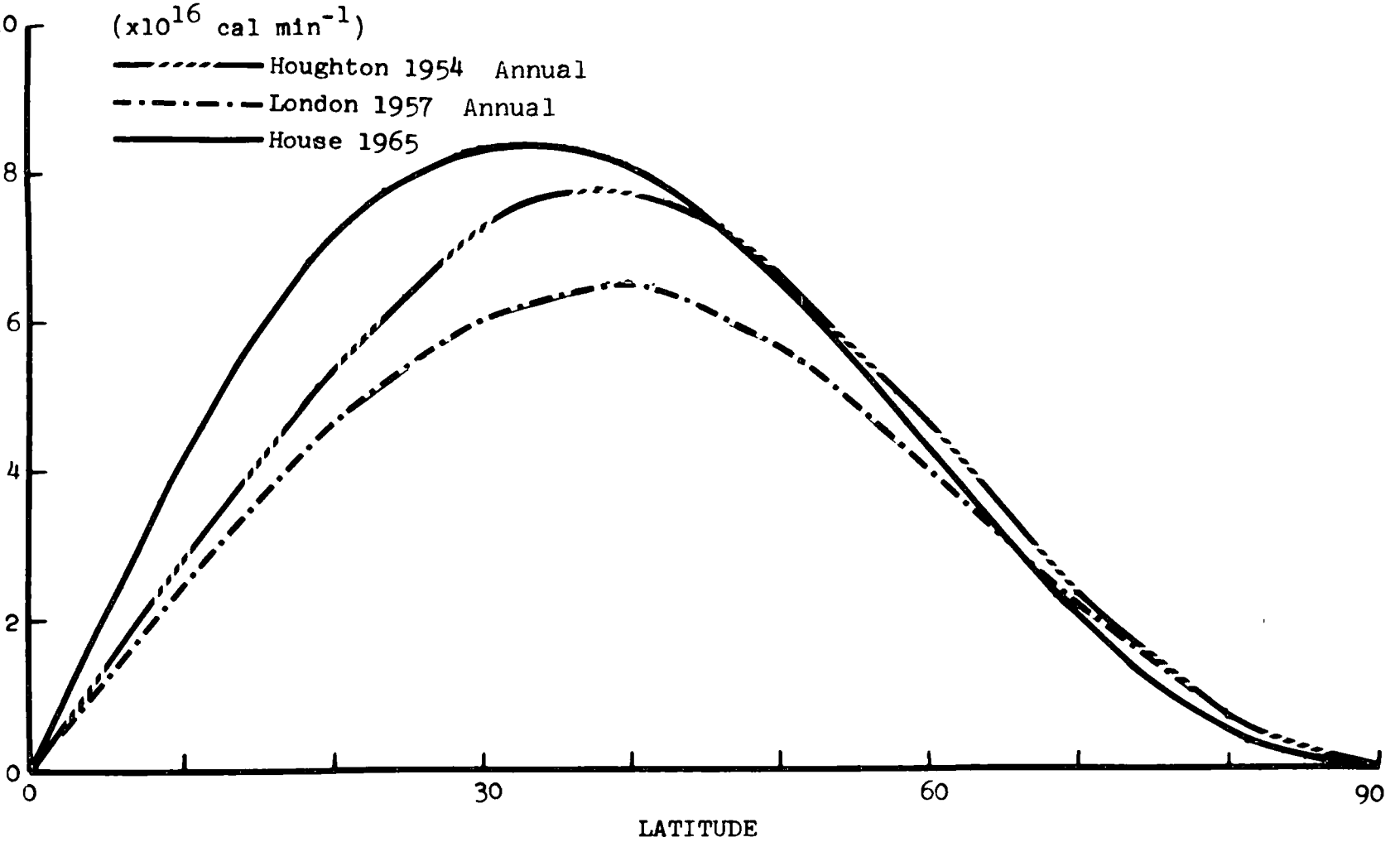

Figure 19

The Flux of Total Heat as Required by the Radiation Balance.

good poleward of 50°; however, the TIROS IV results indicate that the heat transport equatorward of 40° is greater, about 40 per cent larger across latitude 20°. This is a result of the larger input of energy in tropical latitudes due to the lower tropical values of albedo.

Table 3 is a summary of transport calculations, indicating the latitude and magnitude of maximum heat transport.

Table 3

SUMMARY OF PLANETARY TRANSPORT CALCULATIONS

	Maximum Transport	*Latitude*
Simpson (1928)	5.6×10^{16} cal min^{-1}	35°
Simpson (1929)	7.1 "	38°
Baur, Philipps (1935)	6.3 "	37°
Houghton (1954)	7.7 "	38°
Lettau (1954)	7.8 "	$\sim$ 30°
London (1957)	6.6 "	35-40°
Bandeen (1964)	9.8 "	36°
HOUSE (1965)	8.4 ± 0.8 "	$33.5° \pm 1.5°$

It is interesting to note historically that the estimates of heat transport increase with time, and that the latitude of maximum transport moves equatorward. The results of this study indicate a maximum heat transport of $8.4 \pm 0.8 \times 10^{16}$ cal min^{-1}

at latitude $33.5 \pm 1.5°$. The uncertainty in these values is based on the maximum possible systematic error discussed in Section 4.31.

Lettau's analysis is in closest agreement with the values of this study, both in terms of the transport as well as latitudinal position. Houghton's transport result is within the error limits of this study, but his position of maximum heat flux is at a higher latitude. The overall agreement with the satellite results is remarkable.

Included in the summary of Table 3 are the recent results of Bandeen, it. al. (1964), on one complete year of TIROS VII observations. Their results for the heat transport are 17 per cent larger than the value found in this study. They give no indication of the accuracy of their calculations.

A climatological comparison of satellite observations of LWR from EXPLORER VII and TIROS IV are shown in Figure 18. The EXPLORER VII results (House, 1962), are based on six months of EXPLORER VII data (December 1959 thru May 1960). An important feature in the comparison is that the meridional variation of both curves are virtually the same, which indicates that the gradient of LWR is consistent for the two different years of observation. Slightly higher values are indicated in subtropical latitudes by EXPLORER VII. The difference between the observations is within the error limits of the TIROS IV measurements.

V. CONCLUSIONS

This thesis has examined the radiation balance of the earth, based on TIROS IV satellite measurements. The following conclusions briefly summarize the results:

1. Accurate measurements of the solar and terrestrial radiation streams using a single sensing system are possible, providing the satellite orbit has a precessional period relatively long compared with the movement of weather systems.

2. Previous estimates of the meridional distribution of long-wave radiation agree remarkably well with satellite measurements.

3. Earlier estimates of the planetary albedo are confirmed. However, the meridional distribution of measured albedo values shows lower values in tropical latitudes and higher values at middle and polar latitudes than are indicated by previous estimates.

4. Because of 3. above, satellite measurements of the net radiation distribution with latitude require a larger transport of heat from tropical latitudes than previously estimated.

5. Satellite measurements of net radiation during the period March, April and May indicate the possibility that the earth-atmospheric system is in a state of radiative equilibrium.

APPENDIX

DERIVATION OF THE FUNCTION Cos $^{*}\emptyset$

The function Cos $^{*}\emptyset$ geometrically weights the direct SWR, R_S, which is incident to the area viewed by the satellite. The zenith angle of the sun, $\emptyset$, at a point on the earth in Figure 2, varies as much as 50° within the satellite's field of view. Because the cosine of $\emptyset$ is not linear, the function Cos $^{*}\emptyset$ is a weighted average of all possible cones of solid angle dw, and the cosine $\emptyset$ value of the sun's rays to the area viewed by the cone. Let us define Cos $^{*}\emptyset$ with respect to the zenith angle of the sun's rays, $^{*}\emptyset$, at the subsatellite point S. The weighted average is

$$\text{Cos}\ ^{*}\emptyset = \frac{\sum_{i=1}^{k} \text{Cos}\ \emptyset_i\ dw_i}{\sum_{i=1}^{k} dw_i} = \frac{\sum_{i=1}^{k} \text{Cos}\ \emptyset_i\ dw_i}{\beta},$$

where k is the possible number of solid angle cones defined by β.

A comparison of Cos $^{*}\emptyset$ with cosine $^{*}\emptyset$ is shown in Figure 20. The function Cos $^{*}\emptyset$ is greater than zero at $^{*}\emptyset = 90°$, the sunset line on earth. One would expect this since half of the area viewed by the satellite is still in the sunlit portion of the earth. The function Cos $^{*}\emptyset$ is zero only at the shadow transition positions of the orbit.

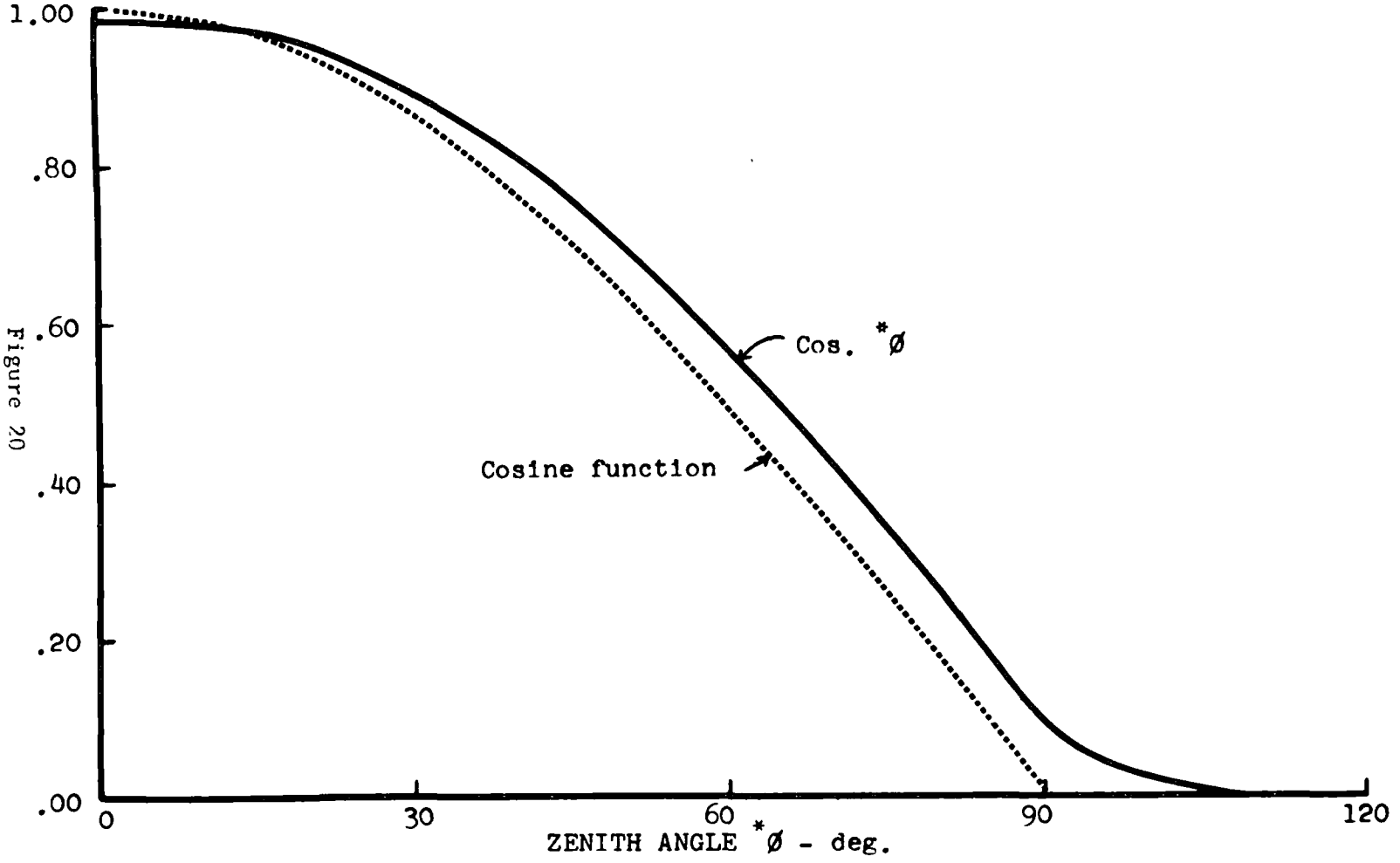

Figure 20

Variation of the Correction Cos. *ø with the Zenith Angle of the Sun at Subsatellite Point.

REFERENCES

Astling, E. G., and L. H. Horn, 1964: An analysis of Diurnal Variations in TIROS II Radiation Data. Annual Report, Grant WBG-10, Department of Meteorology, The University of Wisconsin.

Bandeen, W. R., M. Halev, I. Strange, 1964: A radiation climatology in the visible and infrared from the TIROS meteorological satellites. Paper, presented at the International Radiation Symposium, Leningrad, Aug., 1964.

Baur, F., and H. Philipps, 1934, 1935: Der Warmehaushalt der Lufthulle der Nordhallekugel im Januar und Juli und Feit der Aquinoktien und Solstein. Gerlands Bietr. Geophysik, 41, 160 - 207, and 45, 82 - 132.

Bignell, K. J., 1962: Heat balance measurements from an earth satellite - an analysis of some possibilities. Roy. Meteor. Soc., 231 - 244.

Fritz, S., 1949a: The albedo of the planet earth and of clouds. J. Meteor., 6, 277 - 282.

Godson, W. L., 1958: Meteorological applications of earth satellites. Roy. Astron. Soc. of Canada, 52, No. 2, 49 - 56.

Houghton, H. G., 1954: On the annual heat balance of the northern hemisphere. J. Meteor., 11, No. 1, 1 - 9.

House, F. B., 1962: The long-wave radiation climatology from EXPLORER VII satellite. Paper presented at the Conference on Utilizing Meteorological Satellite Data, Madison, Wisconsin, Nov., 1962.

Johnson, F. S., 1954: The solar constant. J. Meteor., 11, No. 1, 431 - 439.

Lettau, H. H., 1954: A study of the mass, momentum, and energy budget of the atmosphere. Archiv fur Meteorologie, Geophysik, und Bioklimatologie, Series A, Band 7, 133 - 157.

London, J., 1957: A study of the atmospheric heat balance. Final Report, Contract AF 19 (122) - 165, Research Division, College of Engineering, New York University.

Malkevick, M. S., V. M. Pokras, and L. I. Yurkova, 1962: Measurements of radiation balance on the satellite EXPLORER VII. Iskusstvennye Sputniki Zemli, No. 14, 105. Translated by R. E. Daisley, 1963: Planet. Space Sci., 11, 839 - 865.

NASA Staff Members, 1963: TIROS IV Radiation Catalog and User's Manual, Aeronomy and Meteorology Division, NASA Goddard Space Flight Center, 250 pp.

Simpson, G. C., 1928: Further studies in terrestrial radiation. Mem. R. Meteor. Soc., 3, No. 21, 1 - 26.

-------- 1929: The distribution of terrestrial radiation. Mem. R. Meteor. Soc., 3, No. 23, 53 - 78.

Sparkman, B. B., 1964: Experimental analysis of the TIROS hemispheric sensor. Master's thesis, Department of Meteorology, The University of Wisconsin.

Stroud, W. G., and W. Nordberg, 1956: Meteorological measurements from a satellite vehicle, in Scientific Uses of Earth Satellites, James A. Van Allen, ed., University of Michigan Press, Ann Arbor.

Suomi, V. E., 1958: The radiation balance of the earth from a satellite, Annals of the IGY, VI, 331 - 340.

---------- 1961: The thermal radiation balance experiment on board EXPLORER VII, NASA Tech. Note D, 608.

Wark, D. Q., G. Yamamoto and J. H. Lienesch, 1962: Methods of estimating infrared flux and surface temperatures from meteorological satellites. J. Atmos. Sci., 19, No. 1, 369 - 384.

Wexler, H., 1960: Satellites and Meteorology. WMO Bulletin, 9, No. 1, 2 - 7.

Widger, W. K., I. R., and C. N. Tovart, 1957: Utilization of satellite observations in weather analysis and forecasting, Am. Meteor. Soc. Bul., 38, No. 9, 521 - 533.

White, F. D., 1963: The radiative factor in the mean meridional circulation of the Antarctic atmosphere during the polar night. Ph.D. Thesis, Department of Meteorology, The University of Wisconsin.